AGU PUBLICATIONS

JGR

Journal of Geophysical Research: Atmospheres

RESEARCH ARTICLE
10.1002/2017JD026622

Key Points:
- Majority of the schemes overestimate convective updraft speed and radar reflectivity aloft
- Spread in updraft velocity is consistent with spreads in both cold pool intensity and latent heating
- Updraft velocity variability between microphysics schemes is largely attributed to ice-related parameterizations

Supporting Information:
- Supporting Information S1

Correspondence to:
J. Fan,
jiwen.fan@pnnl.gov

Citation:
Fan, J., et al. (2017), Cloud-resolving model intercomparison of an MC3E squall line case: Part I—Convective updrafts, *J. Geophys. Res. Atmos.*, *122*, 9351–9378, doi:10.1002/2017JD026622.

Received 9 FEB 2017
Accepted 24 JUL 2017
Accepted article online 11 AUG 2017
Published online 6 SEP 2017

Cloud-resolving model intercomparison of an MC3E squall line case: Part I—Convective updrafts

Jiwen Fan[1], Bin Han[1,2], Adam Varble[3], Hugh Morrison[4], Kirk North[5], Pavlos Kollias[5,6], Baojun Chen[2], Xiquan Dong[7], Scott E. Giangrande[8], Alexander Khain[9], Yun Lin[10], Edward Mansell[11], Jason A. Milbrandt[12], Ronald Stenz[13], Gregory Thompson[4], and Yuan Wang[14]

[1]Pacific Northwest National Laboratory, Richland, Washington, USA, [2]School of Atmospheric Sciences, Nanjing University, Nanjing, China, [3]Department of Atmospheric Sciences, University of Utah, Salt Lake City, Utah, USA, [4]National Center for Atmospheric Research, Boulder, Colorado, USA, [5]Department of Atmospheric and Oceanic Sciences, McGill University, Montreal, Quebec, USA, [6]School of Marine and Atmospheric Sciences, Stony Brook University, Stony Brook, New York, USA, [7]Department of Hydrology and Atmospheric Sciences, University of Arizona, Tucson, Arizona, USA, [8]Environmental and Climate Sciences Department, Brookhaven National Laboratory, Upton, New York, USA, [9]The Institute of the Earth Science, The Hebrew University of Jerusalem, Jerusalem, Israel, [10]Department of Atmospheric Sciences, Texas A&M University, College Station, Texas, USA, [11]NOAA/OAR/National Severe Storms Laboratory, Norman, Oklahoma, USA, [12]Meteorological Research Division, Environment and Climate Change Canada, Dorval, Canada, [13]Department of Atmospheric Sciences, University of North Dakota, Grand Forks, North Dakota, USA, [14]Division of Geological and Planetary Sciences, California Institute of Technology, Pasadena, California, USA

Abstract An intercomparison study of a midlatitude mesoscale squall line is performed using the Weather Research and Forecasting (WRF) model at 1 km horizontal grid spacing with eight different cloud microphysics schemes to investigate processes that contribute to the large variability in simulated cloud and precipitation properties. All simulations tend to produce a wider area of high radar reflectivity ($Z_e > 45$ dBZ) than observed but a much narrower stratiform area. The magnitude of the virtual potential temperature drop associated with the gust front passage is similar in simulations and observations, while the pressure rise and peak wind speed are smaller than observed, possibly suggesting that simulated cold pools are shallower than observed. Most of the microphysics schemes overestimate vertical velocity and Z_e in convective updrafts as compared with observational retrievals. Simulated precipitation rates and updraft velocities have significant variability across the eight schemes, even in this strongly dynamically driven system. Differences in simulated updraft velocity correlate well with differences in simulated buoyancy and low-level vertical perturbation pressure gradient, which appears related to cold pool intensity that is controlled by the evaporation rate. Simulations with stronger updrafts have a more optimal convective state, with stronger cold pools, ambient low-level vertical wind shear, and rear-inflow jets. Updraft velocity variability between schemes is mainly controlled by differences in simulated ice-related processes, which impact the overall latent heating rate, whereas surface rainfall variability increases in no-ice simulations mainly because of scheme differences in collision-coalescence parameterizations.

1. Introduction

Deep convective clouds have profound impacts on the hydrologic cycle and atmospheric radiation budget [*Arakawa*, 2004]. The former is a result of heavy convective precipitation and widespread stratiform rainfall, while the latter is due to the extensive spatial coverage of anvil clouds. Complicated microphysical and dynamical processes involved in deep convective clouds and gaps in our understanding are impediments to accurate model simulations. In general, it is expected that high-resolution models with more complete and less parameterized physics are more faithful in reproducing nature, but such models still involve many assumptions [*Khain et al.*, 2015]. In recent model intercomparison studies of tropical convective clouds with cloud-resolving models (CRMs) and limited area models (LAMs) [*Fridlind et al.*, 2012; *Zhu et al.*, 2012], all models drastically overestimated radar reflectivity and vertical velocity in deep convective updrafts but underestimated stratiform rainfall [*Varble et al.*, 2011, 2014a, 2014b]. At the same time, there was a large spread in modeled radar reflectivity and deep convective updraft velocity within various CRM and LAM simulations. Different model dynamics and microphysics parameterizations were employed in these intercomparison studies (and in most previous intercomparison studies), making it difficult to attribute model differences to specific factors, although it was clear that microphysics schemes modulated the magnitude of biases relative to observations.

Even within the same dynamical model, results have shown a general sensitivity of CRM deep convection simulations to different cloud microphysics schemes, which often produce large differences in storm structure, dynamics, precipitation, and anvil characteristics [e.g., *Li et al*., 2009a, 2009b; *Morrison et al*., 2009; *Morrison and Milbrandt*, 2015; *Fan et al*., 2015; *Khain et al*., 2015]. This spread of deep convective cloud properties leads to a large uncertainty in assessing aerosol impacts on these clouds as the magnitude and even the sign of changes in updraft strength and surface precipitation with aerosol loading often vary, depending upon the particular model and microphysics parameterization used [e.g., *Van den Heever and Cotton*, 2004; *Fan et al*., 2012, 2013; *Khain et al*., 2015]. In particular, recent studies have shown large differences in simulating aerosol effects on deep convection using bulk versus bin microphysics parameterizations [*Lebo and Seinfeld*, 2011; *Fan et al*., 2012, 2013; *Wang et al*., 2013; *Khain et al*., 2015]. However, there is a lack of studies about the dominant factors and processes producing sensitivities to different microphysics schemes. It is reasonable to believe that improved understanding and ability to reliably simulate aerosol effects on deep convection is contingent upon a reduction in uncertainty in simulating deep convective systems more generally. Therefore, it is important to understand the dominant processes and factors that contribute to these model differences first, which can then focus future observational needs and model improvements. In addition, validating, improving, and developing numerical weather prediction and general circulation model (GCM) parameterizations often employ CRM simulations as benchmarks [e.g., *Xu et al*., 2002; *Randall et al*., 2003; *Suhas and Zhang*, 2015]. The large spread of CRM and LAM deep convective cloud simulations makes it difficult to define "benchmarks" and limits their use in parameterization development.

Squall lines are linearly organized mesoscale convective systems (MCSs) that commonly occur in the tropics and midlatitudes. A key aspect of squall-line organization and maintenance is the balance between the cold pool strength and low-level environmental wind shear [e.g., *Rotunno et al*., 1988; *Weisman and Rotunno*, 2004; *Bryan et al*., 2006; *Takemi*, 2007]. *Rotunno et al*. [1988] proposed a theory that the interaction between low-level environmental vertical wind shear (Δu) and cold pool intensity (C) controls organization and lifetime of quasi-linear convective systems (hereinafter referred to as Rotunno-Klemp-Weisman (RKW) theory), where cold pools are maintained primarily through rain evaporation in convective and mesoscale downdrafts. According to RKW theory, the optimal state of a squall line (i.e., $C/\Delta u = 1$) exists when horizontal vorticity associated with the cold pool circulation balances horizontal vorticity associated with low-level vertical wind shear in the environment ahead of the squall line, producing upright convective updrafts. If shear is too weak relative to the cold pool, the line will tilt in the upshear direction. A rear-inflow jet often forms as a response to a convective circulation having upshear tilt and horizontal pressure gradients [*Weisman and Rotunno*, 2004]. On the other hand, if the cold pool is weak relative to shear, the squall line tilts in the downshear direction. Therefore, changes in cold pool strength via changes in microphysical processes can alter the strength and organization of squall lines. For example, *Morrison et al*. [2012] showed that a more aggressive raindrop breakup scheme led to stronger cold pools due to greater evaporation, which facilitated faster squall line propagation, larger MCS size, and greater updraft mass flux for the midlatitude squall line case they simulated. Many studies have also shown squall-line convective intensity and precipitation structure to be sensitive to parameterization of cloud microphysics [e.g., *Khain*, 2009; *Li et al*., 2009a, 2009b, *Morrison et al*., 2009; *Morrison and Milbrandt*, 2015; *Baldauf et al*., 2011]. The general conclusion based on these studies is that bin microphysics and two-moment bulk schemes predict the spatial structure of rain in squall lines better than single-moment bulk schemes, while domain mean rain rate can vary by up to a factor of two between different microphysics schemes [*Khain et al*., 2015].

This intercomparison study focuses on major differences produced by different microphysical schemes and examines dominant underlying factors responsible for these differences by using simulations of a squall line MCS event over the U.S. Southern Great Plains (SGP). To realize our goals, a constrained approach is employed in which simulations with different cloud microphysics schemes (including one-moment bulk, two-moment bulk, and bin schemes) are run with the same dynamical core using exactly the same model setup except for the parameterization of microphysics. This is different from many previous model intercomparison studies in which different models have been run based on a common case [e.g., *Redelsperger et al*., 2000; *Xu et al*., 2002; *Fridlind et al*., 2012].

The squall-line MCS case simulated in this study occurred on 20 May 2011, during the Midlatitude Continental Convective Clouds Experiment (MC3E) [*Petersen and Jensen*, 2012; *Jensen et al*., 2016], which was supported

by both the U.S. Department of Energy Atmospheric Radiation Measurement Program (ARM) and NASA's Global Precipitation Measurement mission ground validation program in north-central Oklahoma from 22 April to 6 June 2011. Detailed ground-based and aircraft cloud dynamical and microphysical observations are available for this case [*Mather and Voyles*, 2013; *Jensen et al*., 2016], which has been a focus of several recent studies [e.g., *Tao et al*., 2013, 2016; *Giangrande et al*., 2014; *Fan et al*., 2015; *Kumjian et al*., 2016; *Marinescu et al*., 2016; *Van Lier-Walqui et al*., 2016; *Saleeby et al*., 2016; *Fridlind et al*., 2017]. Section 2 includes a more detailed description of the case and the relevant observations used in this study. Convective updrafts are key elements of deep convective clouds and are the focus of this paper, which is the first part of a multi-part study. A follow-on study will focus on the properties of the stratiform region.

The rest of the paper is organized as follows: section 3 describes model and experiment design. In section 4, we first discuss and evaluate simulated precipitation, cold pool, and updraft properties. We then describe the spread of simulated updraft intensity across the microphysics schemes and the main factors leading to the spread. Following that, we examine how the differences in updrafts and precipitation are related to micro-physical processes and how ice-related microphysics parameterizations contribute to them. Section 5 presents conclusions and discussion.

2. Case Description and Observations

The squall-line MCS event on 20 May 2011 during the MC3E field campaign was oriented northeast-southwest with surface precipitation extending for approximately 1000 km along the line and ~200 km perpendicular to the line at its peak size around 1100 UTC. The squall line evolved from two lines during the developing stage between 0100 and 0600 UTC. As shown in Figure 1a, a northern segment was located in Kansas and a southern segment was located in western Oklahoma and northern Texas. The two lines began to interact around 0630 UTC. The southern line dominated and the system developed into a quasi-linear MCS with a leading line of deep convection and an extensive region of trailing stratiform precipitation (Figure 1b). The near-surface atmospheric environment ahead of the squall line has a cloud condensation nucleus (CCN) number concentration of 320 cm^{-3} at a supersaturation of 0.4% [*Fan et al*., 2015].

This case was extensively sampled by ground-based remote-sensing instrumentation, aircraft, and satellites. A multi-Doppler radar 3-D wind field retrieval is a crucial data set used for evaluation of simulated convective properties in this study. The Doppler radar network around the ARM SGP Central Facility (CF) included a 6.3 GHz C-band Scanning ARM Precipitation Radar (CSAPR) located approximately 20 km north of the SGP CF [e.g., *Atmospheric Radiation Measurement Program (ARM) Climate Research Facility*, 2010; *Giangrande et al*., 2014]. During the 20 May 2011 squall line event, nearby well-calibrated operational Vance Air Force Base, OK (KVNX) and Wichita, KS (KICT) NEXRAD WSR-88D 2.8-GHz (S-band) [e.g., *Whiton et al*., 1998] radars routinely collected reflectivity and Doppler velocity measurements. This triplet of CSAPR and WSR-88D radar volumes matched fairly well in time, and therefore, wind field retrievals could be performed as long as the time offset between their respective volume scans was less than 60 s. Radial velocity observations from CSAPR, KVNX, and KICT were assimilated in a three-dimensional variational algorithm capable of retrieving wind fields that satisfy the input velocity observations and anelastic mass continuity simultaneously, among other physical constraints [*North et al*., 2017]. The wind retrievals were performed on a regular 0.5 km spaced Cartesian grid surrounding the SGP CF covering 125 km × 100 km × 10 km in meridional, zonal, and vertical distances, respectively. The retrieval is averaged to 1 km horizontal gridding before making comparisons with model output.

The other observations employed for evaluation are radar reflectivity (Z_e) and precipitation rate. Z_e comes from the National Severe Storms Laboratory (NSSL) three-dimensional (3-D) radar mosaic reflectivity data set, a data product that combines all available radars (NEXRAD, TDWR, and gap radars) gridded at 0.01° (~1 km) horizontal and varying vertical resolutions (0.25 km–2 km) with 10 min temporal frequency [e.g., *Zhang et al*., 2005]. For precipitation, three rainfall accumulation products are considered: NEXRAD National Mosaic and Multisensor Quantitative Precipitation Estimate (NMQ Q2), a bias-corrected NEXRAD Q2, and an hourly Arkansas-Red Basin River Forecast Center (ABRFC) product [e.g., *Young et al*., 2000; *Zhang et al*., 2011]. The NMQ Q2 product suite includes gridded radar reflectivity moments used to generate conventional rain-rate estimates at 5 min intervals and 1 km gridding resolution. The bias-corrected NMQ Q2 products (1 km grid resolution) are available at hourly intervals, with accumulation errors adjusted by nearby

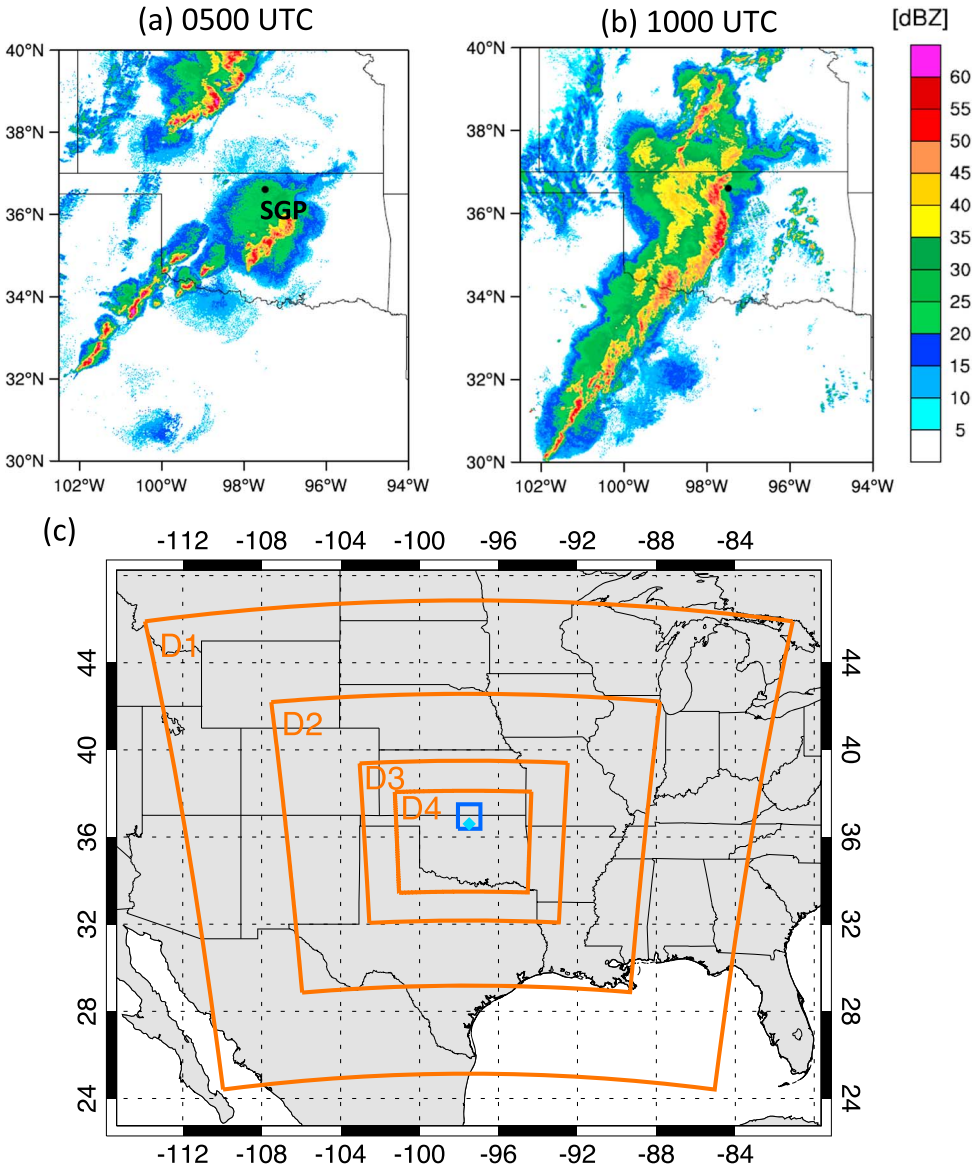

Figure 1. Composite NEXRAD radar reflectivity at (a) 0500 and (b) 1000 UTC, with (c) the model domains used. D1, D2, D3, and D4 represent Domains 1, 2, 3, and 4, respectively. The cyan dot is the SGP Central Facility (CF) location, and the small blue box represents the multi-Doppler retrieval domain.

rain gauge measurements. The ABRFC products combine NEXRAD radar precipitation estimates with rain gauge reports at a horizontal grid spacing of 4 km, placing additional emphasis on gauge accumulations.

Our motivation to consider several independent observational rainfall products was based on known observational uncertainties in conventional radar-based rainfall estimates during MC3E [*Xie et al.*, 2014]. Overestimation of rainfall accumulations during Oklahoma's warm season is common when implementing single parameter Z-R relations (as in simplified forms of the NMQ Q2 products) because of natural variability and/or possible hail or melting layer contamination [e.g., *Giangrande and Ryzhkov*, 2008; *Gourley et al.*, 2010; *Stenz et al.*, 2014; *Wang et al.*, 2016]. Methods that incorporate rain gauge reports, as in ABRFC products, can help mitigate radar system biases (miscalibration) and accumulation errors. Therefore, these products may provide improved hourly estimates when the rainfall is well sampled by those gauges. ABRFC may poorly sample convective rainfall rates even if implementing additional gauge controls, due to factors including the coarse spatial resolution of rain gauge measurements, gauge undercatchment in higher winds, and enhanced radar reflectivity measurements because of hail contamination.

The well-distributed Oklahoma Mesonet sites [e.g., *Fiebrich et al*., 2006] provide robust spatially distributed data sets for surface meteorological parameters including pressure, temperature, wind speed, and direction. The MESONET stations are dense spatially (one or more per county) and cover almost all of Oklahoma. These data are used for evaluating the simulations, particularly the squall-line cold pool evolution.

3. Model Description and Simulation Design

All simulations are performed using the fully compressible and nonhydrostatic Advanced Research Weather Research and Forecasting (WRF) model version 3.4.1. Its vertical coordinate is a terrain-following hydrostatic pressure coordinate. The grid staggering is the Arakawa C-grid. The model uses the Runge-Kutta third-order time integration schemes, and the third and fifth-order advection schemes are selected for the vertical and horizontal directions, respectively. The positive definite option is employed for advection of moist and scalar variables. The model uses a time-split small step for acoustic modes. Eight cloud microphysics schemes are employed for intercomparison including one-moment bulk, two-moment bulk, and bin representations. The schemes used are Morrison (MORR), Milbrandt and Yau (MY2), WSM6 (WSM6), Fast Spectral-Bin Microphysics (FSBM), National Severe Storms Laboratory (NSSL), Predicted Particle Properties (P3), Thompson (THOM), and Texas A&M University Two-moment Bulk Microphysics (TAMU). A short description for each scheme is provided in Text S1 in the supporting information. The prognostic variables in each scheme with references are listed in Table 1. FSBM, NSSL, and P3 explicitly calculate condensation and evaporation based on predicted supersaturation, but all other schemes employ the saturation adjustment approach. Table 2 summarizes the major ice formation parameterizations in each microphysics scheme. For the P3 scheme, although it has been generalized to include a user-specified number of multiple ice-phase categories [*Milbrandt and Morrison*, 2016], only the one-category configuration is used in this study. Note that, although simulations are run with WRF V3.4.1, updates in later versions for a few microphysics schemes (i.e., NSSL, MORR, and MY2) are incorporated (see supporting information for the details).

Real-case simulations are conducted with initial and boundary conditions produced from NCEP FNL (Final) Operational Global Analysis data on a 1° × 1° grid. Four nested domains are utilized with horizontal grid spacing of 27, 9, 3, and 1 km, respectively (Figure 1c). The numbers of horizontal grid points for Domains 1, 2, 3, and 4 are 96 × 91, 181 × 166, 301 × 271, and 601 × 511, respectively. Fifty-one vertical levels are used with a grid spacing of ~60 m at the lowest levels and ~490 m at the uppermost levels. To reduce computation time and size of model output, and to simplify the feedback between the nested domains, the "nest down" approach is used to run the innermost 1 km domain. That is, simulations for Domain 4 are performed separately with initial and lateral boundary meteorological conditions obtained from Domain 3 every 3 h, where Domains 1–3 were run once simultaneously with the standard Morrison microphysics. Simulations are initialized at 0000 UTC on 20 May and run for 18 h.

The Kain-Fritsch cumulus parameterization [*Kain*, 2004] is employed for Domains 1 and 2. We use the Rapid Radiative Transfer Model for application to GCMs shortwave and longwave radiation schemes [*Iacono et al*., 2008], the Noah Land Surface Model [*Chen and Dudhia*, 2001], and the Mellor–Yamada–Janjic (MYJ) planetary boundary layer scheme [*Hong et al*., 2006]. The dynamic time step is 5 s for the innermost Domain 4.

Unfortunately, there are few measurements to guide the choice of aerosol or droplet number concentrations. Aircraft measurements only exist behind the squall line at the rear of the stratiform region late in the squall line life cycle with limited clear-air samplings. Surface-based CCN measurements indicate a concentration of 320 cm^{-3} at ~0.4% supersaturation. Except for FSBM and NSSL that predict droplet number concentration (N_c), N_c is held constant with a clean continental environment default value of ~250 cm^{-3} in all other schemes. For NSSL, aerosol is a single prognostic variable with the initial sea-level value set to be 450 cm^{-3} to obtain typical cloud droplet number concentrations of ~250 cm^{-3} in cloud, consistent with the value set in the other bulk schemes. For FSBM, cloud droplet concentration (N_c) is prognostic and droplet nucleation is calculated from predicted supersaturation and aerosol size distribution based on Köhler theory. The initial aerosol size distribution is determined as $N_{ccn} = cS^k$, where $c = 1500$, $k = 0.308$, and S is the critical superstation for aerosols over each size bin assuming aerosol composition of ammonia sulfate. A uniform vertical aerosol distribution is used to be more consistent with bulk schemes since most of the bulk schemes are configured with a fixed droplet number concentration vertically and horizontally. This aerosol setup yields

Table 1. Summary of the Microphysics Schemes Employed in This Study

Microphysics	Approach	Prognostic Variables[a]	References
MORR	Two-moment	Q_c, Q_r, Q_i, Q_s, Q_h, N_r, N_i, N_s, N_h	*Morrison et al.* [2005]; *Morrison et al.* [2009]
MY2	Two-moment	Q_c, Q_r, Q_i, Q_s, Q_g, Q_h, N_r, N_i, N_s, N_g, N_h	*Milbrandt and Yau* [2005a, 2005b]; *Milbrandt and McTaggart-Cowan* [2010]; *Milbrandt et al.* [2012]
WSM6	One-moment	Q_c, Q_r, Q_i, Q_s, Q_g	*Hong and Lim* [2006]
FSBM	Bin-resolved	Q_c, Q_r, Q_i, Q_s, Q_h, N_c, N_r, N_i, N_s, N_h	*Khain* [2009]; *Fan et al.* [2012]
NSSL	Two-moment	Q_c, Q_r, Q_i, Q_s, Q_g, Q_h, N_c, N_r, N_i, N_s, N_g, N_h, V_g, V_h	*Mansell et al.* [2010]
[b]P3	Two-moment	Q_c, Q_r, Q_{i_tot}, Q_{i_rim}, B_{i_rim}, N_r, N_{i_tot}	*Morrison and Milbrandt* [2015]
THOM	Hybrid one- and two-moment	Q_c, Q_r, Q_i, Q_s, Q_g, N_r, N_i	*Thompson et al.* [2004, 2008]
TAMU	Two-moment	Q_c, Q_r, Q_i, Q_s, Q_g, N_r, N_i, N_s, N_g	*Li et al.* [2008]; *Wang et al.* [2011]

[a]The symbols denote the mass mixing ratios and number concentrations of cloud water (Q_c, N_c), rain (Q_r, N_r), ice (Q_i, N_i), snow (Q_s, N_s), graupel (Q_g, N_g), and hail (Q_h, N_h). In P3, "cloud ice" includes all ice types. V_g and V_h are volume mixing ratios for predicting bulk density for graupel and hail, respectively.
[b]Q_{i_rim} and B_{i_rim} denote the rime mass and volume mixing ratios, respectively.

typical N_c of 500–700 cm^{-3} in convective updrafts and 150–250 cm^{-3} in the stratiform region. Therefore, in convective updrafts, N_c in FSBM is about 2–3 times higher than in other schemes.

Simulations without ice processes ("no-ice") were also conducted to examine the contribution of ice-related microphysical processes to variability of updraft velocity and precipitation across different schemes. These simulations are run for each microphysics scheme in the same way as the simulations with full microphysics, except that ice-related microphysics is turned off. Microphysics and dynamics variables are output with 5 min time frequency for all simulations from 0600 to 1000 UTC.

4. Results

4.1. Rainfall and Cold Pool Properties

The average surface precipitation rates for the time period of 0600–1000 UTC (i.e., the main development period of the squall line) vary by a factor of 1.5 between the different microphysics schemes, with MY2 and THOM on the low end and TAMU and WSM6 on the high end (Figure 2a). The accumulated precipitation during 0600–1200 UTC (excluding the 6 h spin-up time period) averaged over the domain varies by a factor of 1.5 as well from 7.3 mm in THOM to 11.2 mm in WSM6 and TAMU (Table 3). Simulated accumulated precipitation amounts generally fall within the observed range from ABRFC and bias-corrected NMQ Q2, with MY2 and THOM as outliers (the total precipitation from NSSL is only slightly less than the ABRFC accumulation and P3 only slightly more). As expected, nonadjusted radar Q2 accumulations are much larger than the bias-corrected NMQ Q2 (15–30%) and ABRFC amounts (40–100%). As ABRFC accumulations tend to represent the lower end of convective rainfall observational values, MY2 and THOM likely underestimate precipitation since their values are less than ABRFC. Figure 2b shows that MY2 has much lower occurrence of rain rates

Table 2. Ice Nucleation Parameterizations Used by the Microphysics Schemes

Microphysics	Deposition-Condensation Nucleation	Immersion Drop Freezing[a]	Homogenous Drop Freezing
MORR	*Cooper* [1986][b]	*Bigg* [1953]	Instantly freezing at $T \leq -40$°C
MY2	*Meyers et al.* [1992]	*Bigg* [1953]	*DeMott et al.* [1994]
WSM6	Temperature-dependent	*Bigg* [1953]	Instantly freezing at $T \leq -40$°C
FSBM	*Meyers et al.* [1992]	*Bigg* [1953]	*Bigg* [1953]
NSSL	*Phillips et al.* [2007]	*Bigg* [1953]	*Bigg* [1953]
P3	*Cooper* [1986]	Modified *Bigg* [1953]	Instantly freezing at $T \leq -40$°C
THOM	*Cooper* [1986]	*Bigg* [1953]	Instantly freezing at $T \leq -38$°C
TAMU	*Pruppacher and Klett* [1997]	None	*DeMott et al.* [1994]

[a]Besides immersion drop freezing, some schemes including MORR, MY2, P3, and NSSL also implement contact drop freezing following *Cotton et al.* [1986]. However, the current parameterization of contact freezing contributes negligibly to drop freezing.
[b]The same parameterization could be implemented differently. For example, MORR, P3, and THOM all use *Cooper* [1986] for deposition-condensation ice nucleation, but different temperature and supersaturation limits are used (see model descriptions for details).

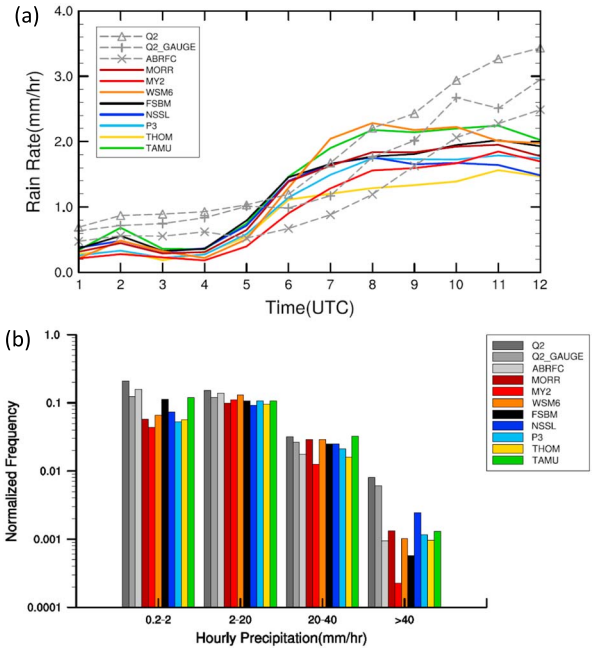

Figure 2. (a) The time series of domain-mean precipitation rate for the simulations and three observational data products (NEXRAD Q2, bias-corrected Q2 denoted by "Q2_Gauge," and ABRFC) from 0100 to 1200 UTC and (b) normalized frequencies of precipitation rates for simulations from 0600 to 1000 UTC and observations from 0700 to 1100 UTC. Frequency is normalized by the total domain grid points, which are regridded to the same 0.04° × 0.04° grid for both simulations and observations. The colors denoting schemes are the same throughout the paper except as specifically noted.

larger than 20 mm h^{-1} than other simulations, and MY2 and THOM have the lowest and second lowest occurrences, respectively, at intermediate rain rates of 20–40 mm h^{-1}.

Figure 2a also shows that simulated systems develop about 1 h earlier than the observed system. The rapid increase of precipitation generally starts at 0500 UTC in the simulations, which is an hour earlier than was observed (0600 UTC). Thus, a 1 h lag is applied to comparisons between the simulations and observations. The 1 h lag is also justified by examining the correlation between the observed rain rate (Q2) and the averaged model results from all simulations: the 1 h lag increases the correlation coefficient from 0.80 (without any lag) to 0.86. Further increasing the lag to 2 h does not improve the correlation much further (0.87). Therefore, for all comparisons with observations starting with Figure 2b and continuing through subsequent figures, the model output is shifted to 1 h earlier than observations. For example, Figure 2b shows the observations from 0700 to 1100 UTC, corresponding to the model output from 0600 to 1000 UTC.

The squall-line reflectivity structure is shown in Figure 3. As described in section 2, the observed squall line developed from two branches, with the southern branch located in western Oklahoma and northern Texas. However, the simulated squall line is dominated by the northern branch that extended into Kansas.

Table 3. Observed and Simulated Accumulated Surface Precipitation (mm) From 0600 to 1200 UTC Averaged Over the Model Domain

NEXRAD Q2	14.24
Bias-corrected Q2	12.19
ABRFC	8.93
MORR	9.61
MY2	8.48
WSM6	11.2
FSBM	9.91
NSSL	8.69
P3	9.00
THOM	7.30
TAMU	11.2

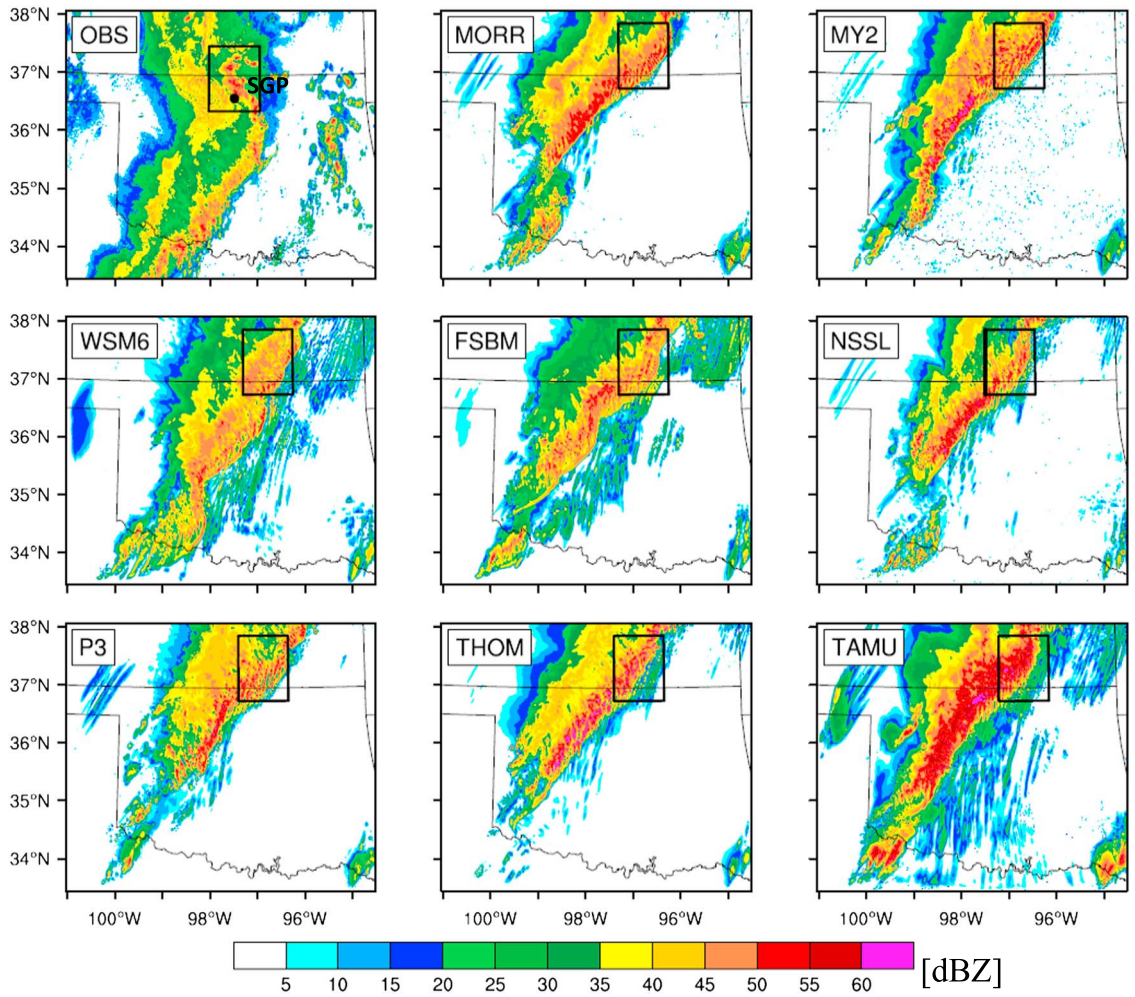

Figure 3. Spatial distribution of composite radar reflectivity for NEXRAD data at 1100 UTC and simulations at 1000 UTC. The Rayleigh radar reflectivity calculation for each scheme is based on assumed and predicted hydrometeor properties. "SGP" on the first panel marks the location of ARM SGP CF. The black boxes denote regions used for comparing convective updrafts.

As shown in Figure 3, the simulated system is shifted northward relative to the observed one at 1100 UTC (1000 UTC for simulations) when the squall line is fully developed. The simulated areas with $Z_e > 45$ dBZ are 17,407 (MORR), 18,959 (MY2), 13,149 (WSM6), 10,410 (FSBM), 10,299 (NSSL), 10,674 (P3), 10,914 (THOM), and 29,268 (TAMU) km^2. All simulations produce a much wider area of $Z_e > 45$ dBZ than the observations (7612 km^2), especially for the MORR, MY2, WSM6, and TAMU schemes. Another distinct feature visible in Figure 3 is dramatically narrower stratiform area in all simulations as compared with observations. Modeled radar reflectivity is also generally overestimated compared to observations in stratiform regions, with FSBM and NSSL as exceptions, and most lack a distinct low-reflectivity transition zone. The second part of this study will focus on these model differences in stratiform precipitation properties.

To evaluate cold pool evolution associated with the squall line, near-surface virtual potential temperature, pressure, and wind speed at Oklahoma MESONET sites over a wide region are analyzed in Figure 4. Sites located between 35–37°N and 96–99°W are grouped into 0900–1000 UTC (Figure 4a) and 1000–1100 UTC periods (Figure 4b) based on the time when the gust front passed over each station, and results are plotted from 2 h before (minus sign at the *x* axis) to 2 h after (plus sign) the gust passage. Model data are processed in the same way, except that the region is shifted to 35.8–37.8°N and 98–95°W and time is shifted to 1 h earlier due to the location and temporal shifts of the simulated events. We use a potential temperature drop of −2 K to define the cold pool edge and approximate gust front location. The simulations and observations produce a virtual potential temperature drop, pressure rise, and wind speed peak associated with passage of the gust

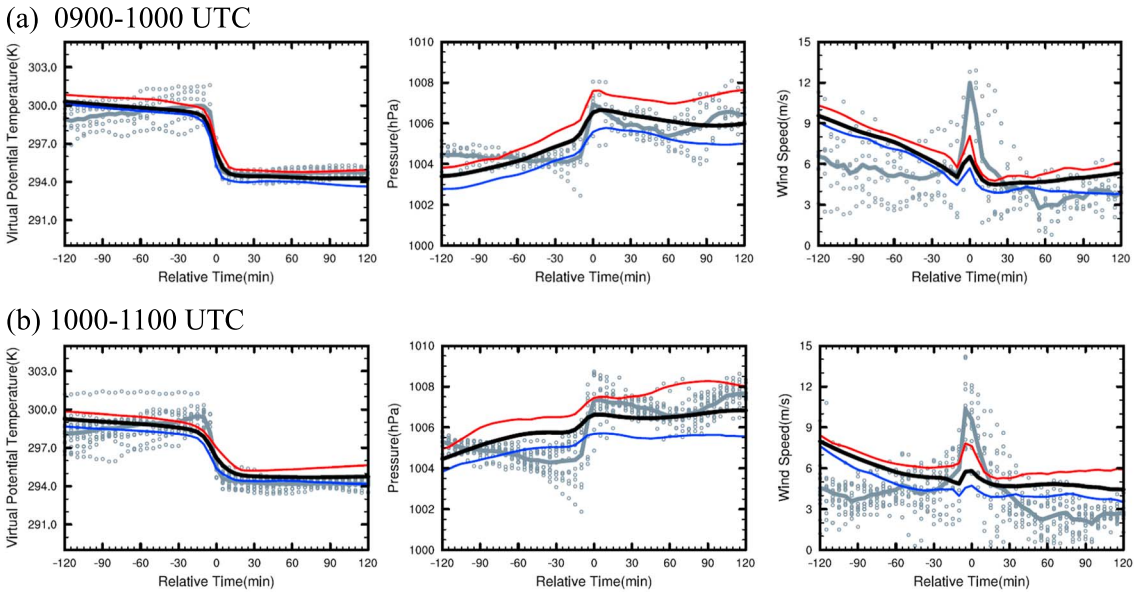

Figure 4. Comparisons of the near-surface virtual potential temperature, pressure, and wind speeds 2 h before (minus sign at *x* axis) to 2 h after (plus sign) the gust front passes a location from the simulations and the MESONET data (gray). For observations, the sites located in the region of (35–37°N, 96–99°W) are grouped into (a) 0900–1000 UTC and (b) 1000–1100 UTC based on the time when the observed gust front passes by. The gray dots denote observations from the sites, and the gray line is the mean values of all sites (8 sites for 0900–1000 UTC and 10 sites for 1000–1100 UTC). Modeled data are processed in the same way except that the region is shifted to 35.8–37.8°N and 98–95°W, and time is shifted to 1 h earlier. The mean of all eight model simulations is shown in black, with the maximum in red and minimum in blue.

front. For the 0900–1000 UTC period, the observed virtual potential temperature drop is reproduced by simulations, but the pressure rise and wind speed peak are lower than observed, which may suggest that simulated cold pools are too shallower. For the 1000–1100 UTC period (Figure 4b), the magnitudes of virtual potential temperature drop, pressure rise, and gust front peak wind speed from simulations are −1.7 K, 0.5 hPa, and 0.9 m s^{-1}, respectively, significantly smaller than observed values of −3.9 K, 2.7 hPa, and 3.6 m s^{-1}, respectively. Note that the conclusions are not affected by the sample size differences between the observations and simulations.

4.2. Convective Updraft Velocity and Radar Reflectivity

4.2.1. Comparison Between Simulations and Observations

The multi-Doppler 3-D wind retrieval allows for evaluation of convective updraft velocity (*w*). Domains are chosen from each simulation (black boxes in Figure 3) with the same size as the multi-Doppler retrieval domain (black box in the first panel of Figure 3), and the comparison is limited to points with $w > 2$ m s^{-1}. The time period of 0900–1100 UTC (0800–1000 UTC for simulations) is chosen for comparison, when the convective portion of the system passes through the multi-Doppler domain. As shown in Figure 5a, the simulations generally overestimate *w* above 5 km altitude, especially for very strong updrafts (99th percentile). The multi-Doppler retrievals may underestimate vertical velocity by 2–4 m s^{-1} (2 m s^{-1} for the 90th percentile and 4 m s^{-1} for the 99th percentile in Figure 5) based on *North et al*. [2017]. Thus, for some schemes such as FSBM and NSSL, the overestimation aloft reduces to 30% or less after considering the potential observational bias. To validate the multi-Doppler retrieval, we compare it with vertical air motion data retrieved from the ARM 920-MHz UHF Radar Wind Profiler (RWP) for the portion of the squall line that passed over the ARM SGP CF [*Giangrande et al*., 2013]. The accuracy of the RWP retrievals is expected to be within 1–2 m s^{-1} in convective updrafts for this case without large hail [*Giangrande et al*., 2013, 2016], so these may be considered more accurate estimates of vertical velocity whenever available. However, RWP data are confined to a single, potentially spatially unrepresentative column, and thus, the 3-D multi-Doppler retrieval is used for evaluation of simulations. The two retrievals show 2–4 m s^{-1} differences at higher altitudes for the 90th percentiles (Figure 6). The multi-Doppler retrievals have significant uncertainty in the upper troposphere (2–4 m s^{-1}) due to radar sampling and methodology limitations, and thus, this level of agreement is considered within the bounds of uncertainty.

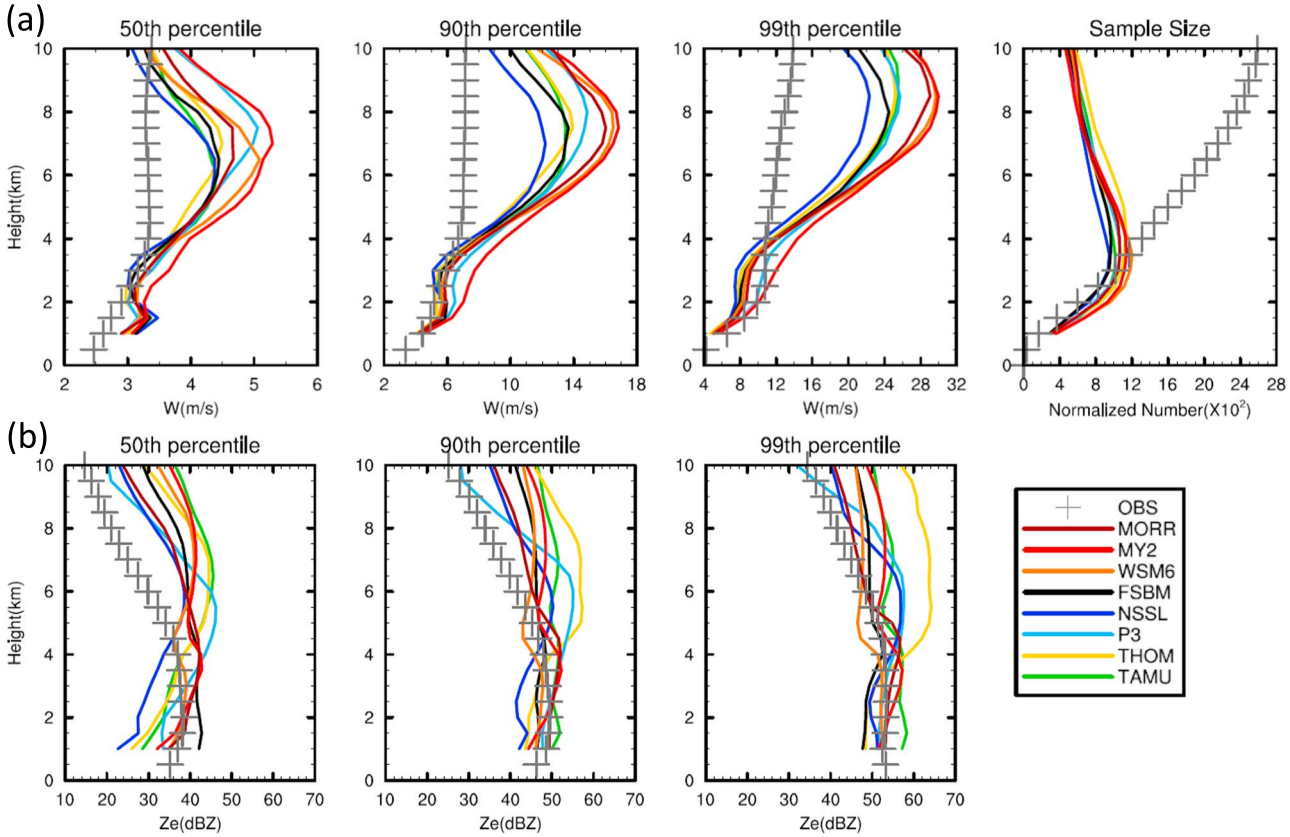

Figure 5. Vertical profiles of (a) updraft velocity and (b) radar reflectivity at the 50th, 90th, and 99th percentiles with multi-Doppler retrievals represented by plus symbols and convective updrafts defined by $w > 2$ m s^{-1}. The last panel of Figure 5a shows the profile of the number of samples, normalized by the number of times in the sampling time period of 0900–1100 UTC for observations and 0800–1000 UTC for simulations. Model output has 5 min frequency, and observations have 5–10 min frequency. (top) The multi-Doppler retrieval domain is shown by the black box in Figure 3. The corresponding model domain has the same size and is shown by the black box in other panels of Figure 3.

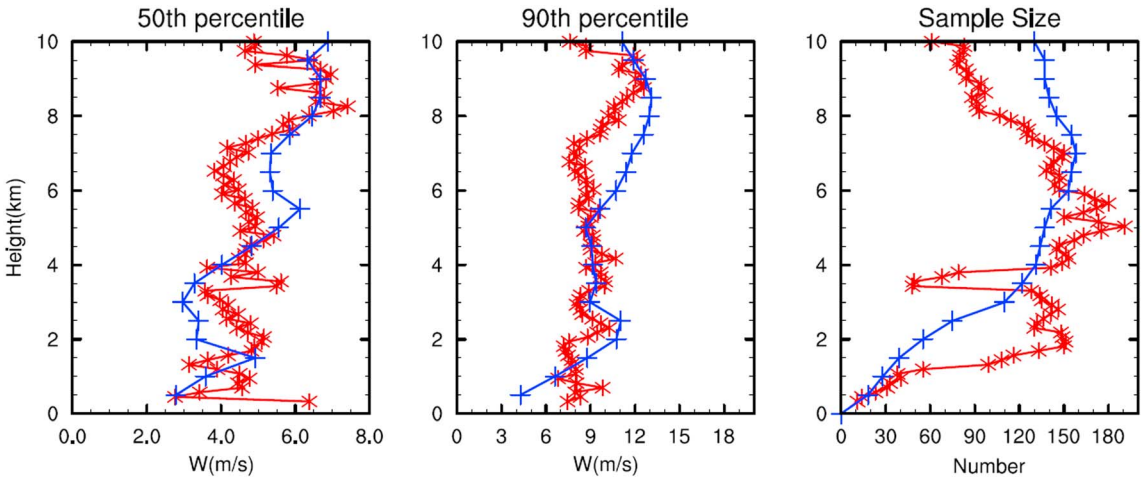

Figure 6. Vertical profiles of updraft velocity at the (left) 50th and (middle) 90th percentiles, with the (right) retrieval sample size from multi-Doppler retrievals (blue) and RWP retrievals (red) at SGP for convective updrafts defined by $w > 2$ m s^{-1}. The RWP observed the convective component of the squall line over a 40 min window (1020–1100 UTC). Multi-Doppler data only have four discrete sampling times during this period, and therefore, multi-Doppler data are used from a west-east cross section ±25 km from the SGP. With this approach, RWP and multi-Doppler sample sizes are similar. The 99th percentile is not shown because of too few samples from the RWP retrieval to give a robust result.

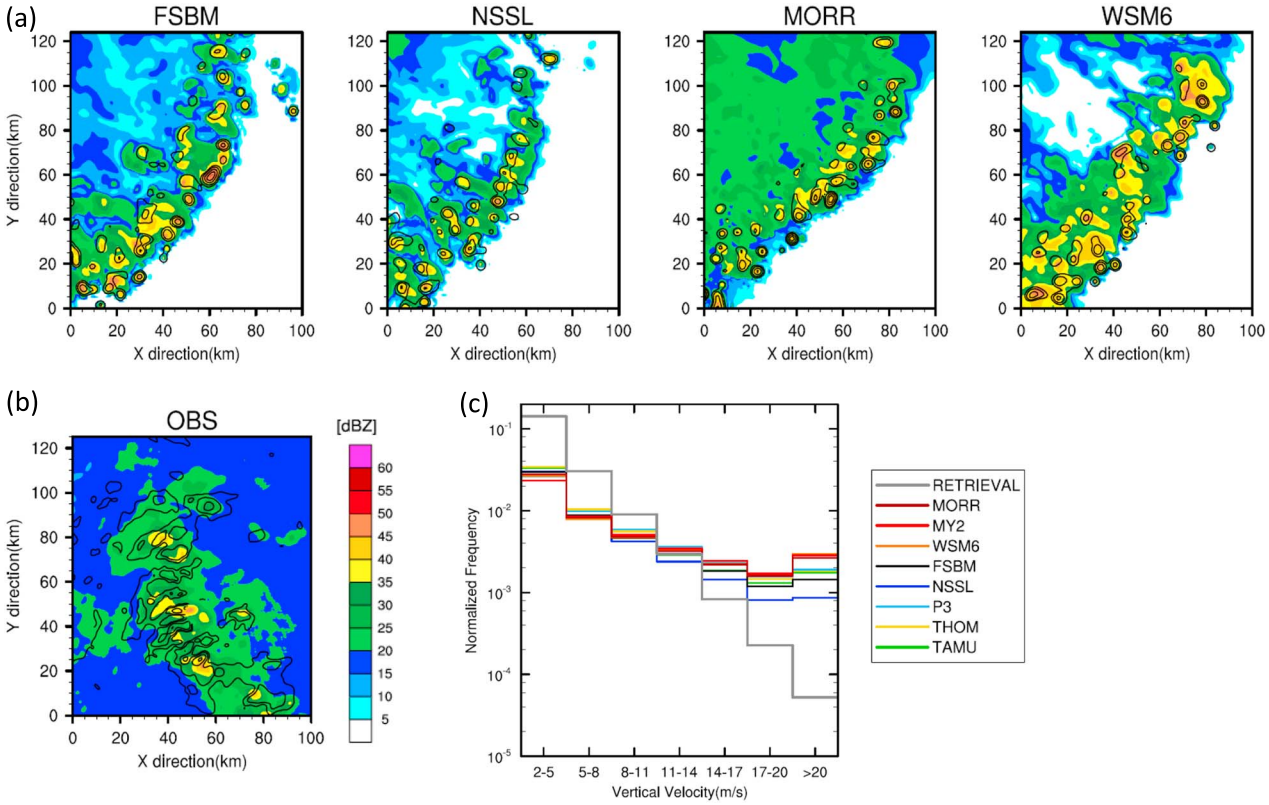

Figure 7. Spatial distribution of 8 km altitude vertical velocity (line contour; start from 2 m s^{-1} and ends at 20 m s^{-1} with a 3 m s^{-1} increment) and radar reflectivity (color fill) from (a) FSBM, NSSL, MORR, and WSM6 simulations at 0940 UTC and (b) multi-Doppler retrievals at 1040 UTC. (c) The normalized frequency of different vertical velocity bins at 8 km altitude are shown for all simulations and the multi-Doppler retrieval.

Total updraft area (i.e., number of grid points with $w > 2$ m s^{-1}) is similar among the simulations at upper levels with 20–40% variability at middle levels but is about 6 times smaller than the area obtained from multi-Doppler retrieval data (last panel of Figure 5a). Furthermore, the vertical profile of updraft area is shaped differently between the simulations and 3-D multi-Doppler retrieval. Updraft area increases with altitude for the multi-Doppler retrievals but decreases above 4 km altitude in the simulations. Increasing the updraft speed threshold from 2 to 5 m s^{-1} for comparison reduces the differences, but the modeled areas remain 2–3 times smaller than retrieved at upper levels despite similar areas at lower levels, with the vertical profile shape remaining the same. Evaluation against available RWP retrievals suggests that multi-Doppler retrievals may overestimate the updraft area by up to a factor of 1.5 for $w > 2$ m s^{-1} at altitudes above 8 km (Figure 6). In addition, the RWP retrievals show that the updraft area decreases with height above 6 km altitude (Figure 6, left), consistent with previous longer term profiler studies of deep convection [e.g., *Kumar et al.*, 2015; *Giangrande et al.*, 2016]. Thus, the multi-Doppler retrievals are possibly biased by radar sampling limitations and methodology that may give excessive coverage of weak convection at upper levels with too little coverage at lower levels. Simulations are qualitatively consistent with RWP retrievals showing a decreasing trend in the updraft area with height, but they still underestimate the updraft area and produce small, intense updraft cores aloft regardless of the microphysics scheme used (Figure 7a). As a result, at upper levels, simulations underestimate the frequency of smaller *w* but overestimate the frequency of larger *w* (Figure 7d). This feature is evident in all simulations and may be associated with model dynamics, particularly the representation of turbulent mixing and diffusion.

Past studies have shown that finer resolution (less than 1 km horizontal grid spacing) better resolves turbulent mixing (e.g., entrainment/detrainment) and can lead to more diluted updraft cores; i.e., the area of weaker updrafts is larger [*Bryan et al.*, 2003; *Lebo and Morrison*, 2015; *Varble et al.*, 2014a]. A sensitivity test using 200 m horizontal grid spacing performed for a domain of 200 km × 200 km nested inside the 1 km grid spacing MORR simulation shows similar results: convective intensity for the strong updrafts (90th percentile

and above) is reduced by 3–5 m s^{-1} above 6 km altitude, and the updraft area is increased by 50%. However, the 50th percentile values are actually larger, due to more occurrences of moderate strength updrafts, in lesser agreement with the multi-Doppler retrieval. Therefore, increasing resolution alone does not fully eliminate model-observation updraft velocity and area differences, a conclusion also reached in *Varble et al*. [2014a]. It is worth mentioning that the updraft cores at upper levels become larger and weaker but not enough to match retrievals, even considering the multi-Doppler retrieval uncertainties.

Small, intense updraft cores in simulations are also associated with high Z_e in all schemes at upper levels (Figure 7a), and as shown in Figure 5b, all simulations overestimate Z_e in updrafts above 5 km altitude with larger overestimates for lower percentiles (i.e., relatively weak updrafts). Overestimation is largest for THOM, resulting from much larger graupel size than in other schemes, as discussed in *Varble et al*. [2014a]. Although not shown, the above conclusions are not affected by the location of the area chosen in simulations for comparison with the observations.

4.2.2. The Simulated Updraft Velocity Spread and Causes

The term spread or variability in this paper refers to the range among the simulations. Large variations in simulated updraft speeds are evident above 5 km altitude for different microphysics schemes (Figure 5a). At upper levels, where the strongest vertical motion and the largest vertical velocity variability occur across schemes, MORR, MY2, and WSM6 produce the strongest updrafts (referred to as the stronger convection group (SCG) hereinafter), while FSBM and NSSL produce the weakest updrafts (referred to as the weaker convection group (WCG) hereinafter; Figure 5a). At 8 km altitude, the strongest updrafts in FSBM and NSSL (i.e., the 99th percentile in Figure 5a) have vertical velocities about 6–8 m s^{-1} less than in MY2 and WSM6.

To understand how different microphysics schemes produce different updraft speeds, we analyze updraft velocity together with key components that impact it (i.e., vertical perturbation pressure gradient acceleration (PPG) and buoyancy acceleration; see Figures 8 and 9). The PPG calculation follows

$$\mathrm{PPG} = -\frac{1}{\overline{\rho}}\frac{\partial p}{\partial z} \tag{1}$$

where p is the perturbation pressure with respect to the horizontal domain average and ρ is the air density. Figure 8 shows that the vertical PPG is positive at low levels in every simulation, presumably associated with mechanical forcing along the cold pool edge. On the other hand, PPG is negative at upper levels, which is associated with dynamic perturbation pressure produced by negative vertical gradients in vertical velocity, as well as buoyant perturbation pressure associated with a negative vertical gradient in buoyancy. Correspondingly, the SCG has more strongly negative PPG acceleration at upper levels than the WCG, attributed to their larger vertical velocities and buoyancy (shown in next paragraph). At low levels, the SCG has larger positive PPG than the WCG. Note that P3, whose convective strength is only slightly weaker than the SCG, has large low-level PPG similar to the SCG, while THOM and TAMU, whose convective strength is only slightly stronger than the WCG, have low-level PPG similar to the WCG.

Above 6 km altitude, the increase in vertical velocity correlates well with increasing buoyancy acceleration (condensate loading included) in each simulation, especially for updrafts with $w > 10$ m s^{-1} (Figure 9). The buoyancy is relatively large for the SCG (i.e., MORR, MY2, and WSM6) and relatively small for the WCG (i.e., FSBM and NSSL). THOM and TAMU, which have intermediate vertical velocities, have large buoyancy acceleration as well, but their low-level PPGs are relatively smaller (Figure 8). Therefore, the updraft velocity variability among simulations correlates well with the variability in both buoyancy and low-level PPG. Both buoyancy and low-level PPG are the largest for the SCG, while both are smallest for the WCG. For the simulations that have intermediate updraft velocity between the SCG and WCG, either buoyancy or low-level PPG values are smaller than those in the SCG.

Buoyancy can be broken down into (1) contributions from temperature, water vapor, and pressure, referred to as "thermal" buoyancy, and (2) condensate loading [e.g., *Houze*, 2014]:

$$B = g\left[\frac{\theta - \overline{\theta}}{\overline{\theta}} + 0.61(q_v - \overline{q_v}) - q_h\right] \tag{2}$$

where g is gravitational acceleration, θ is potential temperature, q_v is water vapor mixing ratio, q_h is total hydrometeor mass mixing ratio, and overbar represents the domain average. The condensate loading

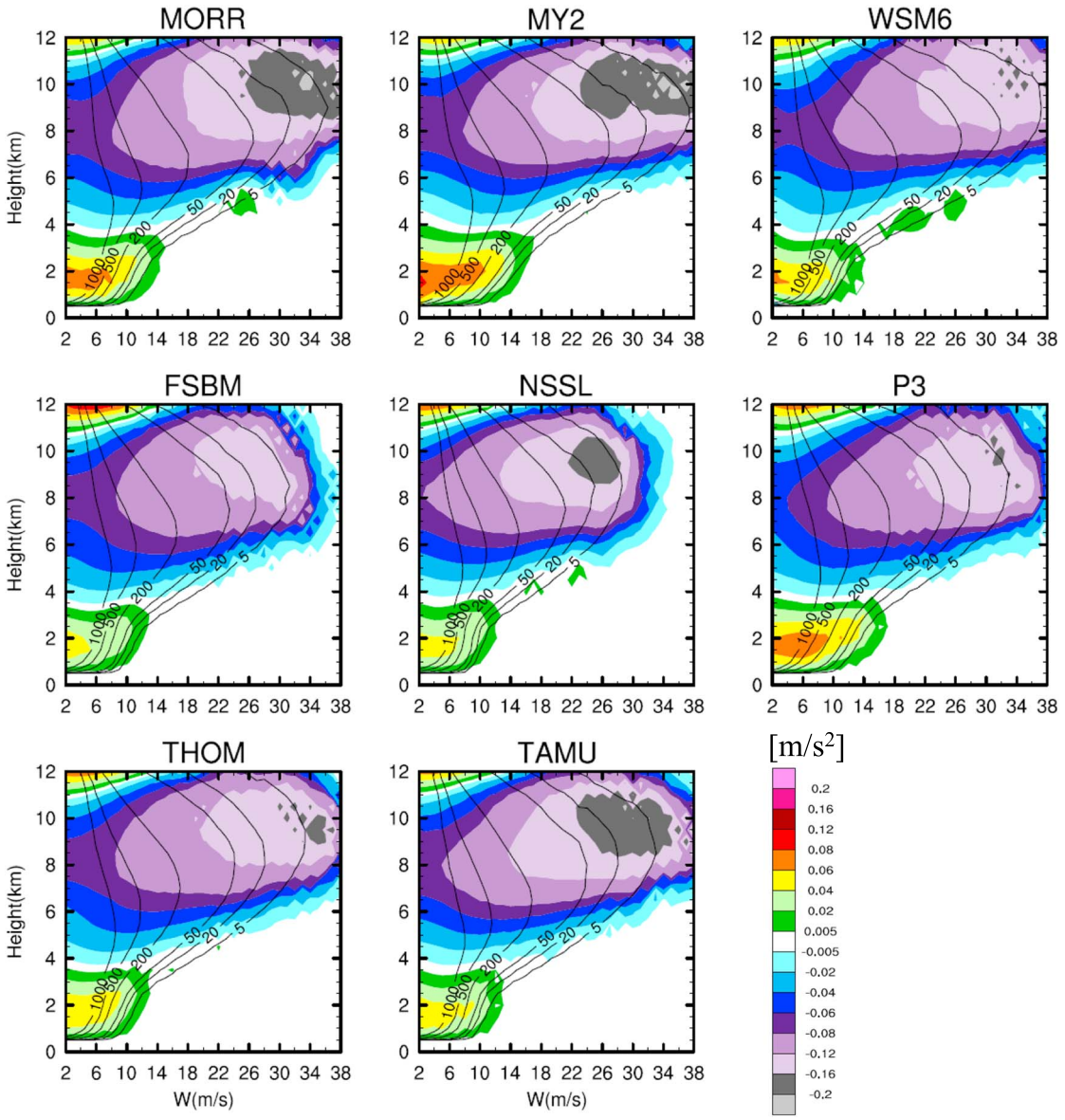

Figure 8. Profiles of the relationship between simulated updraft velocity and vertical perturbation pressure gradient (PPG) acceleration from 0800 to 1000 UTC over the same box shown in Figure 3. The color contours are mean PPG acceleration averaged over all data in each vertical velocity 1 m s^{-1} bin at each height level. The black contours represent sample sizes of vertical velocity at each height level. The reference pressure for the vertical PPG calculation is the domain mean value at each height.

acceleration (the q_h term in equation (2)) is negative (Figure 10) and counters the positive thermal buoyancy (the first two terms in the right side of equation (2)) in updrafts at upper levels as shown in Figure 11. Note that the magnitude of condensate loading acceleration is about half of the magnitude of PPG, and it significantly offsets the positive thermal buoyancy; thus, the buoyancy including condensate loading is only about half of the thermal buoyancy at upper levels (Figure 11 versus Figure 9). Variability in condensate loading acceleration is large (a factor of 2 in the maximum values from the simulations; Figure 10). The SCG has a much larger condensate loading effect than the WCG, especially for the largest w values (especially for $w > 26$ m s^{-1}). Within each simulation, the largest condensate loading occurs with the largest w as well (Figure 10). These results suggest a strong impact of updraft velocity on condensate loading. Moreover, they suggest that differences in condensate loading might not be a significant factor contributing to the differences in vertical velocity since the largest condensate loading (counteracting positive thermal buoyancy) occurs for the SCG, and vice versa for the WCG. Across schemes, P3 has a

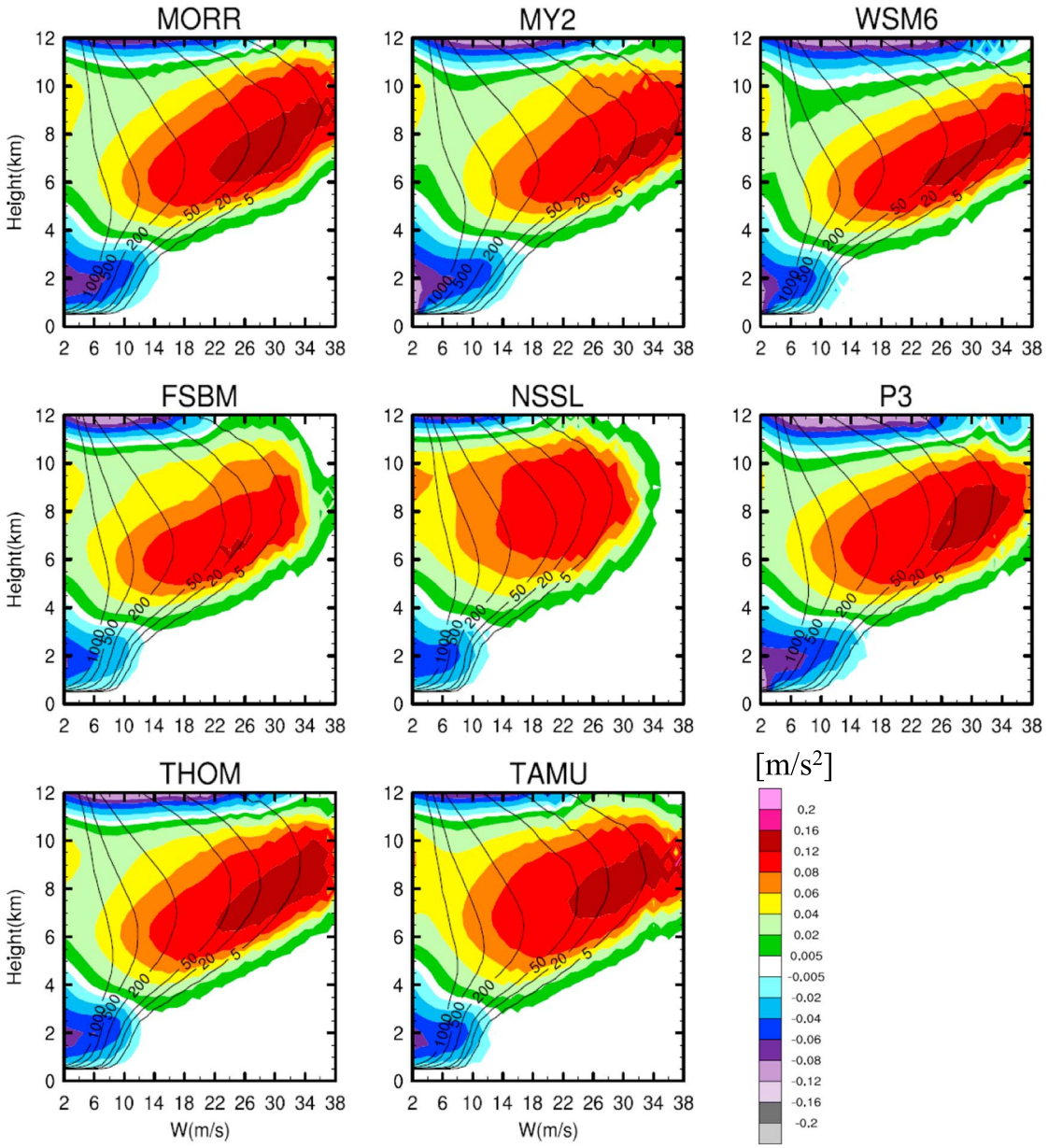

Figure 9. As in Figure 8, except for the buoyancy acceleration incorporating condensate loading. The reference states for potential temperature and water vapor are domain mean values at each height level.

smaller condensate loading effect with relatively stronger updraft intensity and TAMU has a relatively larger condensate loading effect with relatively weaker updraft intensity. Section 4.3 provides further discussion on these points. Overall, the model spread in updraft intensity is consistent with the thermal buoyancy at upper levels.

Latent heating is the main source of thermal buoyancy in updrafts. The relationship of vertical velocity with the net latent heat release (heating plus cooling) presented in Figure 12 shows that the net latent heating for the WCG (i.e., FSBM and NSSL) is indeed smaller than that of the SCG (i.e., MORR, MY2, and WSM6). However, differences in latent heating alone do not fully explain differences in thermal buoyancy among all simulations. For example, WSM6 has the largest latent heating, with values larger than MORR, THOM, and TAMU, while its thermal buoyancy is smaller. Therefore, although latent heating contributes significantly to the thermal buoyancy magnitude in updrafts, other factors such as entrainment may also lead to differences in thermal buoyancy among the simulations.

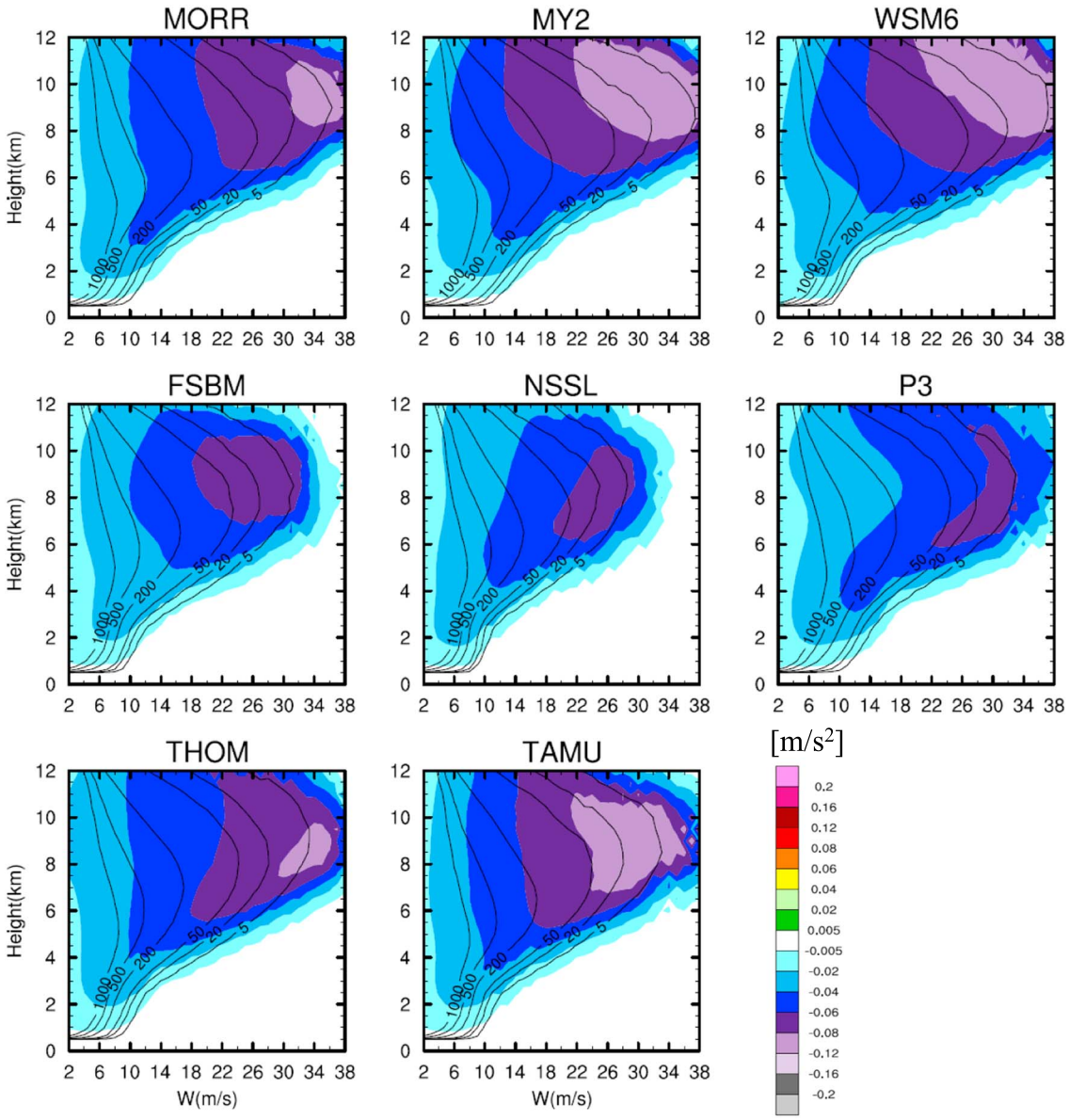

Figure 10. As in Figure 9, except for condensate loading acceleration.

Cold pools contribute to upward acceleration of air through (1) mechanical lifting such as the interactions between a cold pool with low-level wind shear (i.e., RKW theory discussed in the introduction) and (2) the thermodynamic forcing given by the positive anomaly of moist static energy surrounding cold pools [*Tompkins*, 2001]. Based on *Torri et al.* [2015], both mechanisms may be important at different stages of air parcel ascent. We follow *Benjamin* [1968] and *Rotunno et al.* [1988] to calculate cold pool intensity *C*, which has been widely used in recent studies [*Bryan and Morrison*, 2012; *Morrison et al.*, 2012; *Morrison and Milbrandt*, 2015],

$$C^2 = -2\int_0^H B dz \tag{3}$$

where *z* is height; *B* is buoyancy that includes contributions from temperature, vapor, and condensate; and *H* is cold pool depth defined between the surface and the altitude where *B* goes to 0. *C* is taken as an average 0–30 km behind the surface gust front for examining its time evolution. As shown in Figure 13, the cold pool intensity for the SCG is up to 50% stronger than for the WCG at some locations averaged over 0800–1000 UTC (line contours) and up to 20% stronger on average (Figure 14a). The conclusion here is not dependent on the region over which *C* is computed.

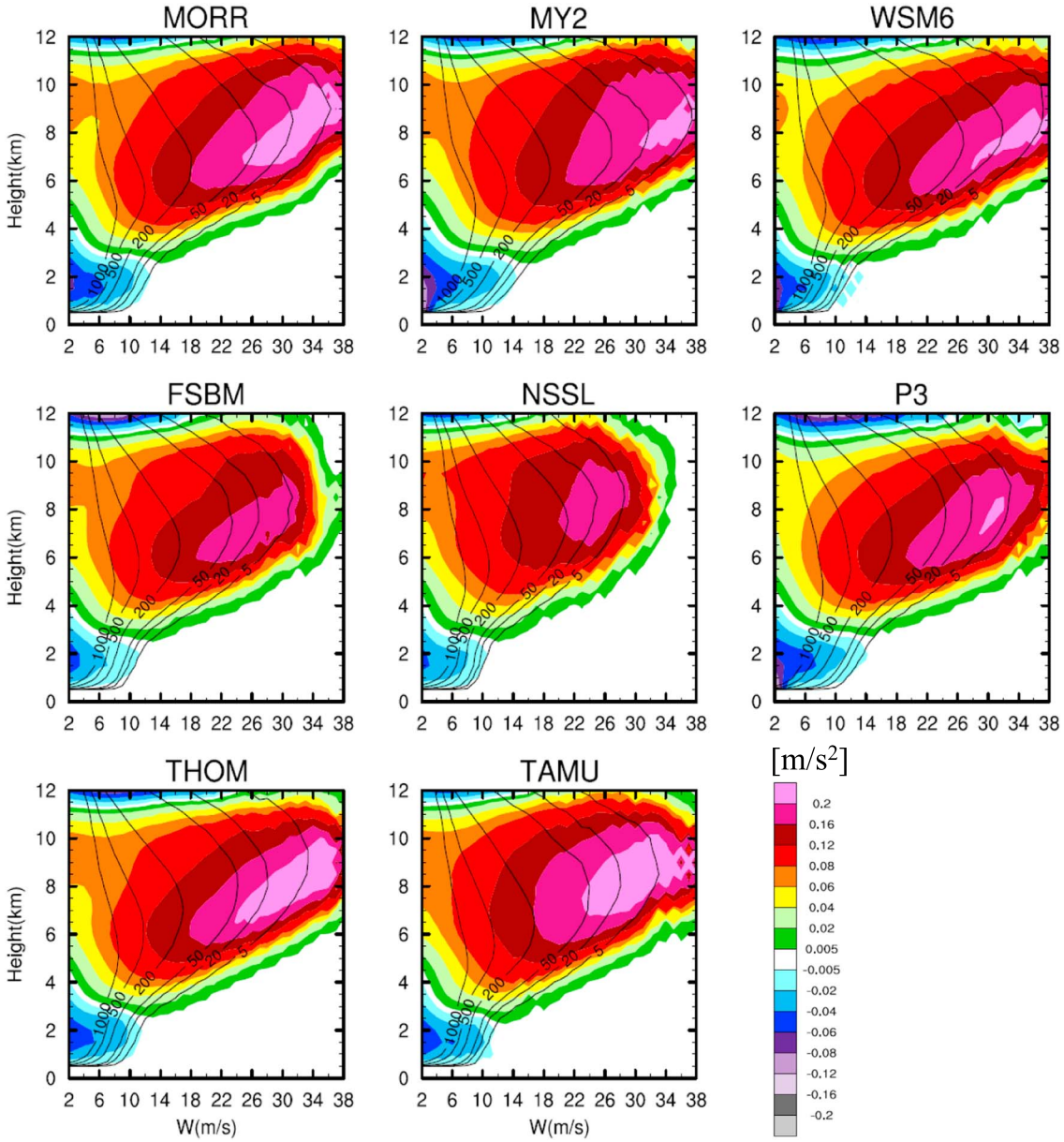

Figure 11. As in Figure 9, except for thermal buoyancy acceleration (i.e., excluding the condensate loading effect).

Despite stronger C for the SCG relative to the WCG, Table 4 shows that $C/\Delta u$ values for the SCG are actually smaller than those for the WCG, which results from 2 to 3 m s^{-1} larger Δu for the SCG as compared to the WCG. Therefore, it seems that stronger cold pool intensity in the SCG is associated with stronger environmental wind shear, leading to stronger horizontal convergence and thus larger dynamic PPG (Figure 13 versus Figure 8), which may contribute to larger updraft velocity. Table 4 also shows that the $C/\Delta u$ values for all simulations are larger than 1.5, which means that the cold-pool circulation overwhelms the ambient vertical shear, the convection tilts upshear, and the system produces a rear-inflow jet [*Weisman and Rotunno*, 2004]. The rear-inflow jet (Δu_j in Table 4) is also a few m s^{-1} stronger for the SCG than for WSG. To account for the effects of rear-inflow jet, *Weisman* [1992] proposed a modified balance state of $C_j/\Delta u = 1$, where $C_j^2 = C^2 - \Delta u_j^2$, Δu_j is the strength of rear-inflow jet, and C_j represents the strength of cold pool circulation including the effects of the rear-inflow jet. Accounting for the effect of the rear-inflow jet makes the $C_j/\Delta u$ ratios smaller than the $C/\Delta u$ ratios, closer to the optimal state of 1 in all the simulations (Table 4). Because the strength of rear-inflow jets in the SCG is larger than in the WCG, and the differences of Δu_j between the SCG and

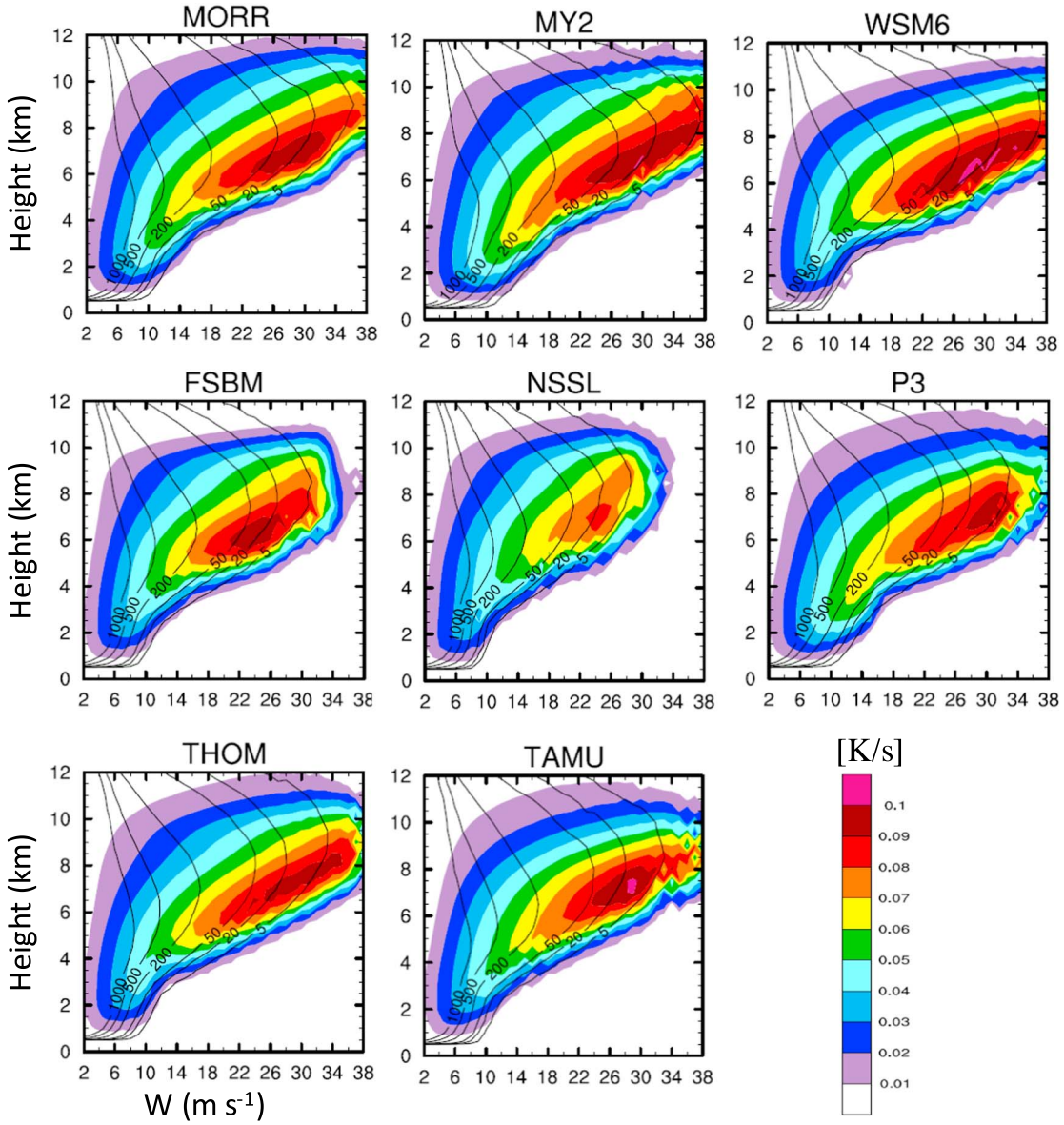

Figure 12. As in Figure 9, except for total latent heating (sum of heating and cooling).

WCG (4–5 m s^{-1}) are larger than the differences of Δu (2–3 m s^{-1}), the convective state is more optimal compared with the WCG, which may help to explain the differences in updraft velocity.

Stronger cold pool intensity corresponds with a larger integrated evaporation rate over the cold pool depth (color contours in Figures 13 and 14a and 14b). FSBM and NSSL (i.e., the WCG) have much weaker evaporation rates compared with the SCG and therefore much weaker cold pool intensity (Figure 14a), where evaporation is dominated by raindrop evaporation (not shown). There is a poor relationship between the cold pool intensity and surface rainfall rate across the simulations with different schemes (Figure 14c), with typical linear correlation coefficients of only 0.2–0.5 with a highest value of 0.6.

Large differences in evaporation rates between different microphysics schemes likely result from different approaches for parameterizing evaporation of both cloud droplets and raindrops and/or from differently simulated raindrop size distributions. The raindrop size distribution differences can be impacted by a large number of microphysical processes, including ice processes since much of the rain forms from melted ice. The impact of ice-related microphysics is discussed further in section 4.4.

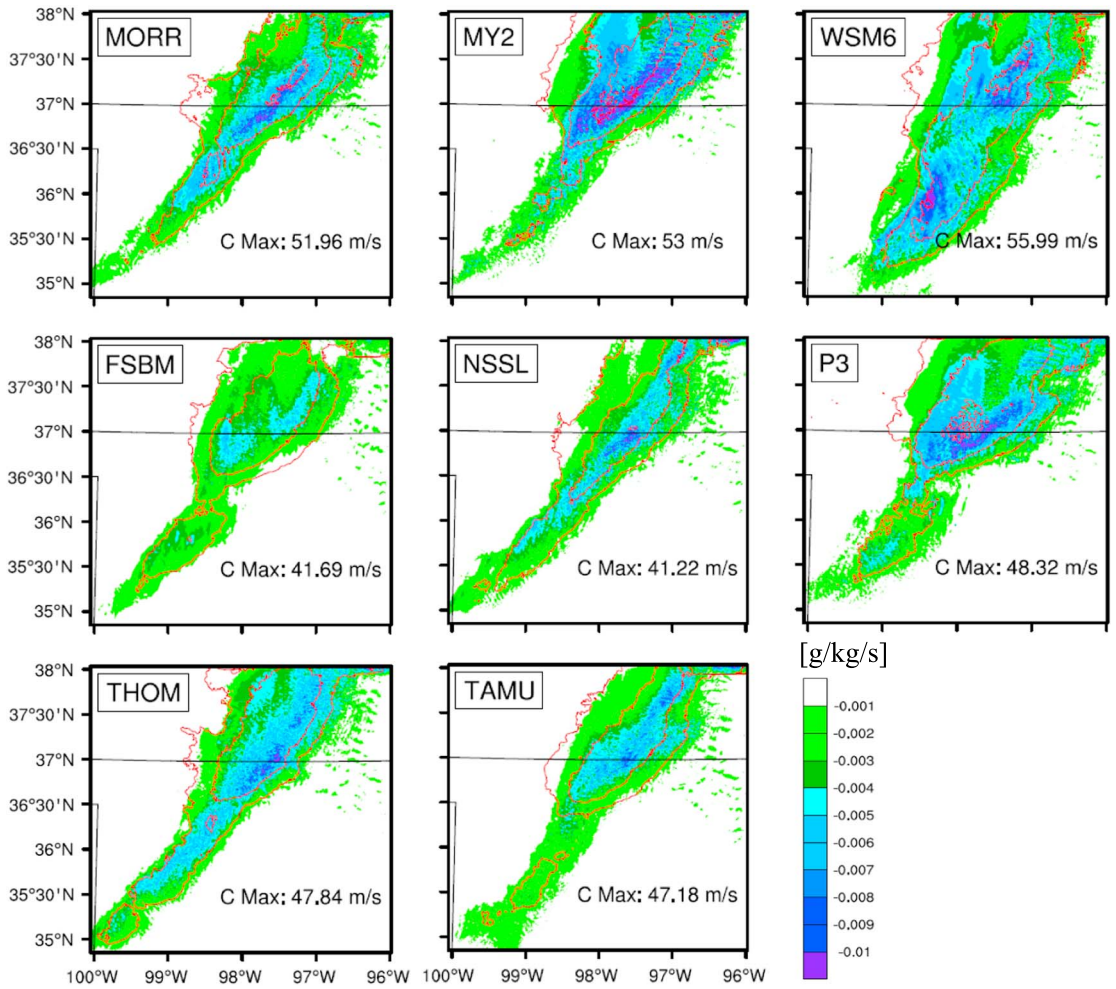

Figure 13. Spatial distribution of cold pool intensity and evaporation rate averaged over 0800–1000 UTC based on the calculation at each grid point at 5 min time frequency. The color fill is cold pool intensity from 10 to 30 m s^{-1} with an interval of 10 m s^{-1}. The red contours denote evaporation rate integrated within cold pool depth. *C* Max is maximum cold pool intensity in the domain averaged over 8–10 h. The evaporation rate accounts for both cloud droplet and raindrop evaporation.

4.3. Microphysical Properties in Convective Updrafts

Since all of the model differences in updraft intensity and precipitation are caused by usage of different cloud microphysics parameterizations, in this section, we examine how the model spread in updraft intensity correlates with microphysical processes and properties. Figure 15 shows the 90th percentiles of latent heating from various microphysical processes in updrafts. Generally, the updraft speed spread correlates with the spread of total latent heating (Figure 15a), as also shown in Figure 12. The SCG (MORR, MY2, and WSM6) has the largest total latent heating. Among the processes producing latent heating, condensation dominates, and differences in condensation heating between different simulations are somewhat consistent with differences in total latent heating and updraft intensity between simulations, particularly above 6 km altitude (Figure 15b). There is a lack of obvious correlation between the spread in simulated updraft speeds and the spread in any specific simulated ice-related microphysical process such as deposition, riming, or drop freezing (Figures 15c–15e). This suggests that complicated interactions among different microphysics processes and feedback between microphysics and dynamics/thermodynamics are at play in causing updraft strength variability between simulations. We do see large variability in deposition heating rate (maximum differences across the simulations of ~120 K/h), a few times larger than the spread in condensation (maximum of ~40 K/h) and riming (maximum of ~30 K/h) heating rates. However, the magnitudes of the heating from condensation or riming are larger at middle levels where updrafts accelerate and the spread in simulated updraft velocities forms, which indicates that they might play a more important role in determining

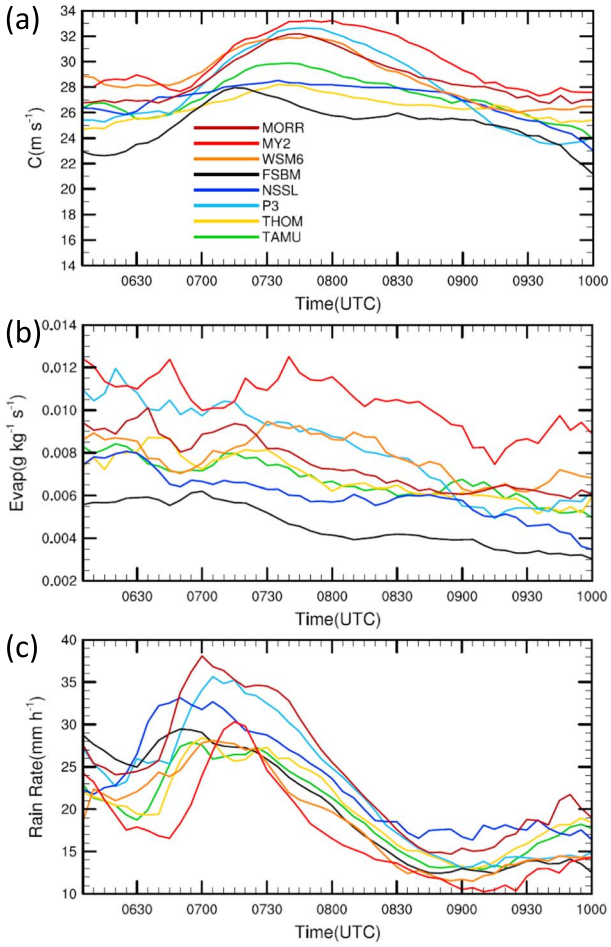

Figure 14. Time series of (a) cold pool intensity, (b) integrated evaporation rate, and (c) precipitation rate. The data are taken as an average 0–30 km behind the surface gust front over a latitude range of 36.8–37.9°N (same as the box chosen for comparing with multi-Doppler retrievals). The integrated evaporation rate is calculated as in Figure 13.

the spread in convective intensity than the deposition heating that peaks strongly at upper levels above the altitude of maximum updraft intensity.

The significantly different microphysical process rates between the simulations result in very different bulk microphysical properties as seen in Figure 16. Stronger convection generally produces larger total

Table 4. Cold Pool Intensity (C), Cold Pool Depth (H), Maximum Vertical Wind Shear (Δu_{max}), and the Ratio of $C/\Delta u_{max}$ Averaged Over 0800–1000 UTC[a]

	MORR	MY2	WSM6	FSBM	NSSL	P3	THOM	TAMU
C [m/s]	29.04	29.82	29.74	25.82	26.07	27.17	26.87	26.94
H [km]	3.90	4.19	4.19	3.16	3.61	3.60	3.91	3.46
Δu	8.54	8.55	9.51	6.85	6.48	7.35	7.17	6.87
$C/\Delta u$	3.40	3.49	3.13	3.77	4.02	3.70	3.75	3.92
Δu_j	20.33	20.46	19.47	15.85	16.18	19.24	18.83	19.69
$C_j/\Delta u$	2.43	2.54	2.36	2.98	3.15	2.61	2.67	2.68

[a]Calculations here follow *Meng et al.* [2012]. Two boxes with a size of 60 km × 30 km were selected that are located behind and in front of the leading edge of the squall line at a distance of 10 km from the leading edge (red boxes in Figure S1). Values of C, H, and Δu_j are averages over the box behind the leading edge. The Δu values are calculated as follows: wind shear is calculated between H and all levels below H using the averaged wind speed at each vertical level over the box ahead of the squall line, with the maximum wind shear value chosen for Δu. Δu_j represents rear-inflow intensity and is calculated the same as Δu except over the box behind the gust front. C_j represents the strength of the cold pool circulation including the effects of the rear-inflow jet. $C_j/\Delta u$ represents the modified balance state of *Weisman* [1992].

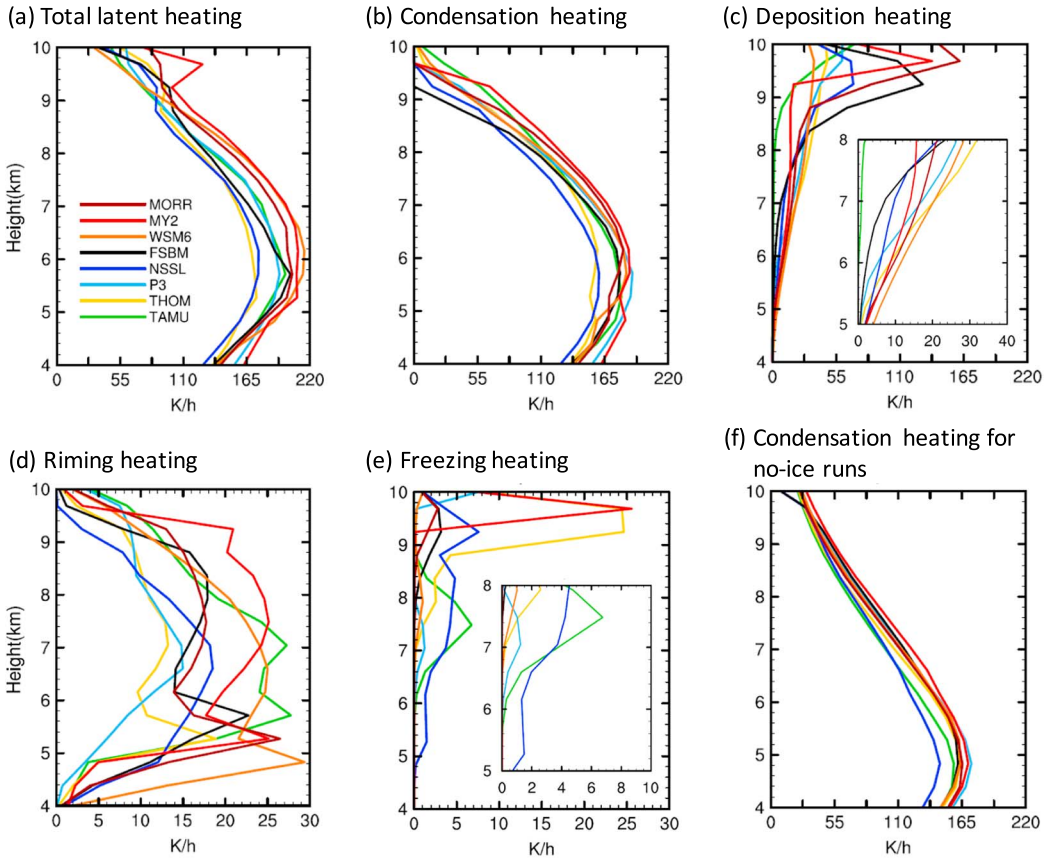

Figure 15. Vertical profiles of the 90th percentile of latent heating rates from (a) all processes, (b) condensation, (c) deposition, (d) riming, and (e) cloud drop freezing for the same updraft points as in Figure 5. Drop freezing in Figure 15e only includes heterogeneous and homogenous cloud drop freezing. (f) Condensation latent heating from the no-ice runs. The inserted panel in Figures 15c and 15e zooms in on 5–8 km altitudes.

condensate mass, so that the SCG has larger total condensate mass than the WCG. As mentioned in section 4.2.2, TAMU produces a similarly large condensate loading effect as the SCG due to significant production of graupel despite weaker updraft intensity, and P3 produces a smaller total condensate mass content despite similarly strong updraft intensity as the SCG because of smaller total ice mass content. A major contributor to the total condensate mass (gray line) above 6 km altitude is graupel (or hail in FSBM and MORR since the hail versions for both schemes were used in this study). Above 6 km altitude, the total condensate mass for the WCG is about 0.5 g kg^{-1} less than those from MY2, WSM6, and TAMU (Figure 16). Graupel is a major contributor to the larger total condensate mass at middle and upper levels in MY2, WSM6, and TAMU, primarily formed from riming (Figure 15).

The larger total condensate mass in WSM6 and TAMU corresponds to greater rainfall rates in these simulations, as discussed in section 4.1, while MY2 and THOM produce the least rainfall. For MY2, despite the similarly large total condensate mass, the smaller rainfall rate is likely a result of larger ice number concentrations (Figure S2 in the supporting information) and relatively small graupel terminal velocity for the specified bulk density of 400 kg m^{-3} from *Ferrier* [1994]. For THOM, snow mass dominates graupel mass (Figure 16), possibly decreasing precipitation efficiency because of the slower fall speed for snow as compared to graupel, which may produce its relatively low rainfall rates. A possible explanation for the large snow mass in THOM is that drop freezing forms more snow than in the other schemes, while the conversion of snow to graupel through riming is smaller by up to 3 orders of magnitude than in the other schemes (not shown). WSM6 has the greatest surface rainfall rates despite limited rain mass at low levels (Figure 16). Greater rainfall rate is often seen in single-moment schemes rather than two-moment and bin schemes [*Khain et al.*, 2015] because of larger sedimentation rates from the single-moment rain size distribution [e.g., *Milbrandt and Yau*, 2005a, 2005b; *Milbrandt and McTaggart-Cowan*, 2010].

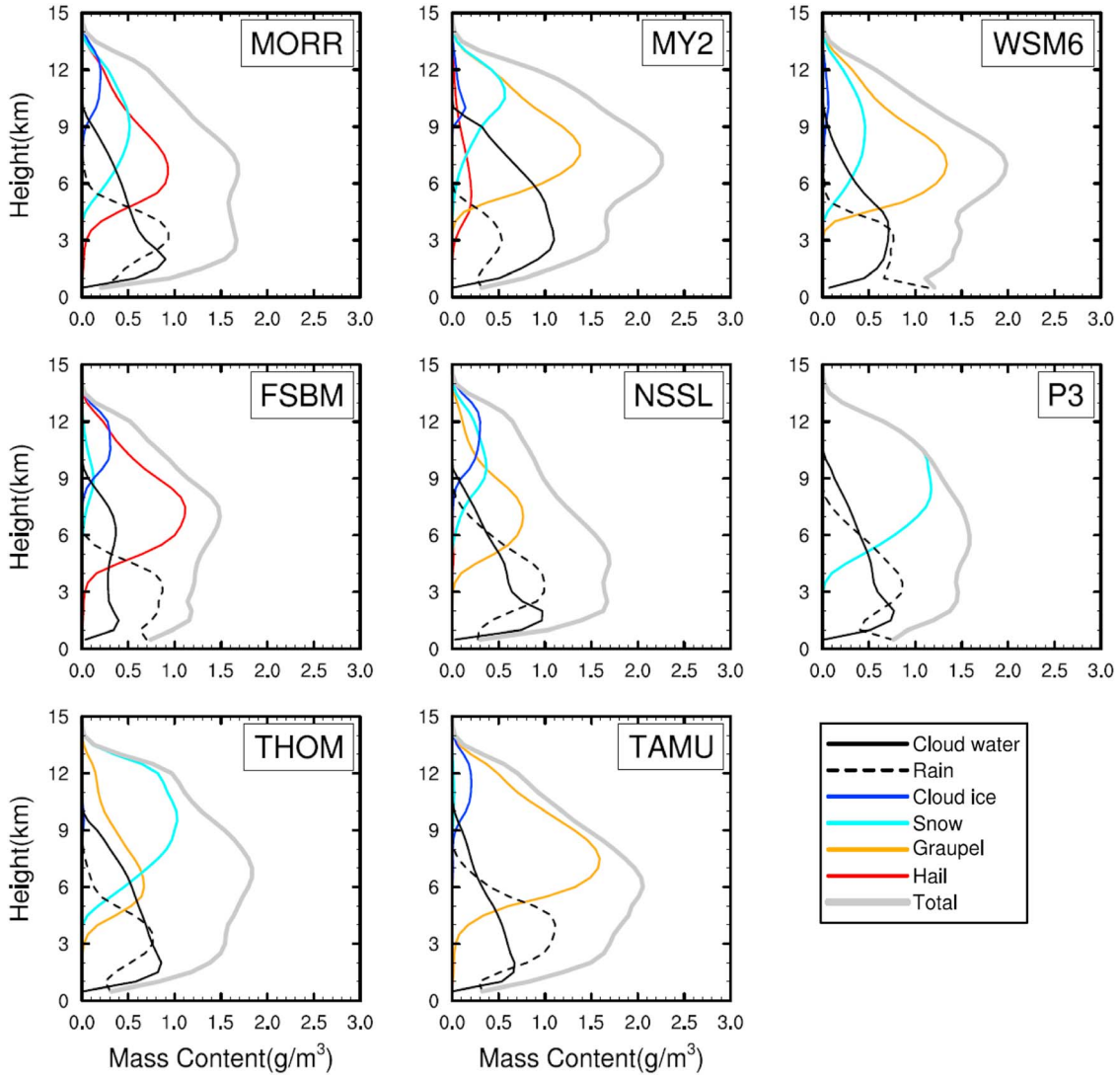

Figure 16. Vertical profiles of hydrometeor mass content averaged over the updraft points with $w > 2$ m s^{-1} from 0800 to 1000 UTC for the entire model domain. The plots for the region in Figure 5 are qualitatively similar. The gray line is total mass content of hydrometeors. Note that P3 has only one ice category, so the cyan line represents ice mass content from all ice particles (not just snow).

All of the bulk schemes that use the saturation adjustment method for calculating droplet diffusional growth predict larger cloud water mass than FSBM, associated with larger mean condensation rates (not shown), possibly associated with the removal of all supersaturation within one time step [*Grabowski and Morrison*, 2017]. Most of the bulk schemes have significant cloud water mass reaching the homogeneous freezing level (−40°C at about 9.7 km altitude). MY2 and THOM, predicting the least surface rainfall, have the most cloud water at low temperatures and hence the largest homogenous drop freezing rates (Figure 15e). In contrast, FSBM does not have significant cloud water at such temperatures, and thus, the homogenous freezing rate is smaller. Among all of the schemes that assume instantaneous homogeneous freezing (Table 2), only THOM predicts a sharp peak in the homogenous freezing rate. A few two-moment schemes (i.e., NSSL, P3, THOM, and TAMU) predict significant rainwater mass content up to an altitude of 8 or 9 km in the updrafts. The schemes that do not predict rainwater above 6 km have either large deposition rates or large riming rates (Figure 15), forming significant graupel or hail mass between 5 and 9 km altitudes.

4.4. Rainfall and Convective Updraft Velocity Without Ice-Related Processes

Since large variability between simulations exists in ice-related process rates such as deposition and riming, removing ice-related processes may reduce the updraft velocity spread. Figure 17 shows that the spread is

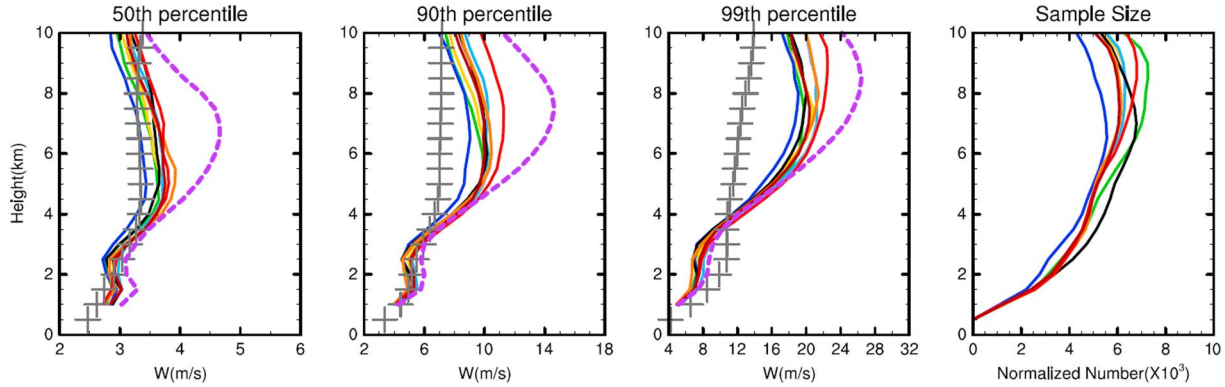

Figure 17. Same as Figure 5a, except showing simulations without ice-related microphysics based on hourly data over the entire model domain. The dashed purple line denotes the mean values from all full microphysics simulations. The plus sign denotes multi-Doppler retrievals. Simulations are represented with the same colors as in Figure 5a.

indeed reduced. Updraft velocity between different schemes varies by less than 1 m s^{-1} for the 50th percentiles and by only 2–3 m s^{-1} for the 90th and 99th percentiles at 8 km altitude with ice-related microphysics turned off (excluding MY2 as an outlier that is discussed later). These differences are much smaller than those from the simulations including ice-related processes (5–8 m s^{-1} for the 90th and 99th percentiles). Given that the magnitude of the updraft velocity is smaller in the no-ice simulations than in the full microphysics runs, we also calculate the normalized spread by dividing the spread in updraft strength with the mean updraft velocity from either the full microphysics or no-ice simulations to compare them in a more quantitative way. At 8 km altitude, the normalized spread for the 90th and 99th percentiles for the no-ice runs is 0.15 and 0.11 (excluding MY2), respectively, while the corresponding values for the full microphysics run are 0.34 and 0.28, respectively. Therefore, the normalized spread is reduced more than half from the full microphysics to no-ice runs (by about one third to half when MY2 is included), which is very significant.

This reduced spread in updraft velocity in the no-ice runs is because of reduced simulation differences in both low-level PPG and middle- to high-level buoyancy accelerations; the maximum differences in the 99th percentile of PPG and buoyancy acceleration are only about 0.06 and 0.03 m s^{-2}, respectively, both of which are about 40% smaller than the corresponding values in the simulations with full microphysics (Figure S3).

Further examination shows reduced differences in cold pool intensity between simulations in the no-ice runs compared to the simulations with full microphysics (Figure 18a versus Figure 14a), which likely explains reduced low-level PPG in the no-ice runs relative to full microphysics runs, with the exception of MY2 (although the reduction in FSBM is not as large as in the bulk schemes). However, the spread of simulated evaporation rates is still large and only slightly reduced compared to that for the full microphysics runs (Figure 18b versus Figure 14b), suggesting that the connection of cold pool intensity with the evaporation rate in the no-ice runs is not as strong as in the full microphysics runs. Therefore, ice-related processes such as melting cause greater correlation between cold pool strength and evaporation rate.

The reduced buoyancy variability between the no-ice runs corresponds well with reduced variability in latent heating between the runs (Figure 15f) relative to the full microphysics runs. There is increased variability in condensation heating among the full microphysics runs compared with the no-ice runs (Figure 15b versus Figure 15f), which is not surprising, given the strong feedback between updraft intensity and condensation (increased vertical velocity directly leads to increased condensation rate). Among all ice-related microphysical processes, the largest variability across schemes is seen in riming below 9 km altitude and deposition and cloud droplet freezing (excluding riming) above 9 km altitude (Figures 15c–15e). Above 9 km altitude, both the variability and absolute values of deposition are about 1 order of magnitude larger than those of cloud droplet freezing, so the contribution of cloud droplet freezing to latent heating variability is minor. Although the variability and absolute values of riming heating are a few times smaller than those from deposition, riming heating is more dominant below the peak updraft strength altitude of 7–9 km where the spread in simulated velocities forms. Additionally, riming heating does not add condensate loading, whereas deposition does, which partially offsets the impact of depositional heating. Riming heating

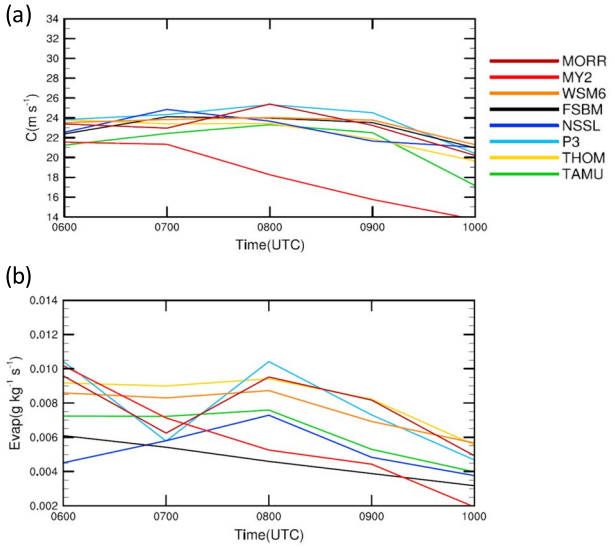

Figure 18. Time series of (a) cold pool intensity and (b) evaporation rate from 0600 to 1000 UTC for no-ice simulation. Data are processed the same way over the same geographical box as in Figure 14.

variability appears to be a contributor to simulated updraft velocity variability (e.g., the SCG has the largest peak riming heating rates below 5.5 km altitude), but condensation differences and, potentially, deposition differences are also important. For example, the relatively large riming heating in TAMU is offset by relatively small condensation and deposition rates, while the relatively small riming heating in P3 is offset by relatively large condensation and deposition rates, and the WCG has modest riming heating with relatively weak condensation and deposition rates. Therefore, the lack of clear correlation between the intersimulation variability in updraft intensity and the intersimulation variability in any one microphysical process likely occurs because several different processes are important, interacting in complex ways and feeding back to the dynamics and thermodynamics. In addition, contributions to this variability in the full microphysics runs (i.e., with ice) from warm microphysical processes cannot be ruled out since condensation and collision-coalescence affect the liquid water mass, size, and number concentrations that reach the mixed-phase region, impacting riming and cloud droplet freezing. Additional study is needed to further isolate the contribution from each of these processes, which could be facilitated by the "piggybacking" methodology [*Grabowski*, 2014, 2015].

Figure 17 also shows weaker convective strength in the no-ice simulations than in the full microphysics simulations, which is represented by an average of all the full microphysics simulations with the dashed purple line. No-ice simulations agree better than full microphysics simulations with the multi-Doppler retrieval denoted by the plus symbols. The shape of updraft area vertical profiles (i.e., sample size of $w > 2$ m s^{-1}) for the no-ice runs (last panel of Figure 17) also mimics that from the RWP retrievals shown in Figure 6. Therefore, ice-related processes contribute significantly to the stronger than observed updraft intensity and vertical profile of updraft area that is different than observed. Much weaker updraft intensity in the no-ice runs appears to result mostly from reduced buoyancy due to reduced latent heating at middle and upper levels relative to full microphysics runs, since the balanced state based on the modified RKW theory ($C_j/\Delta u$) does not change much from the full microphysics to no-ice runs (the cold pool intensity, rear-inflow jet, and low-level wind shear are all reduced in the no-ice runs so that the ratio of $C_j/\Delta u$ does not change much). Small, intense updraft cores occur in the no-ice simulations similarly to those in the full microphysics simulations, further suggesting that this feature is more likely a result of nonmicrophysics-related model issues.

In contrast, variation in surface rain rate is larger in the no-ice simulations than in the simulations with full microphysics (Figure 19a versus Figure 2a), mainly because of large differences in the parameterization of collision-coalescence processes (Figures 19c and 19d) and compensation of these differences from ice-related precipitation in the full microphysics simulations. Mass and number conversion rates from cloud water to rain vary considerably among the different schemes, while condensation and evaporation rates are

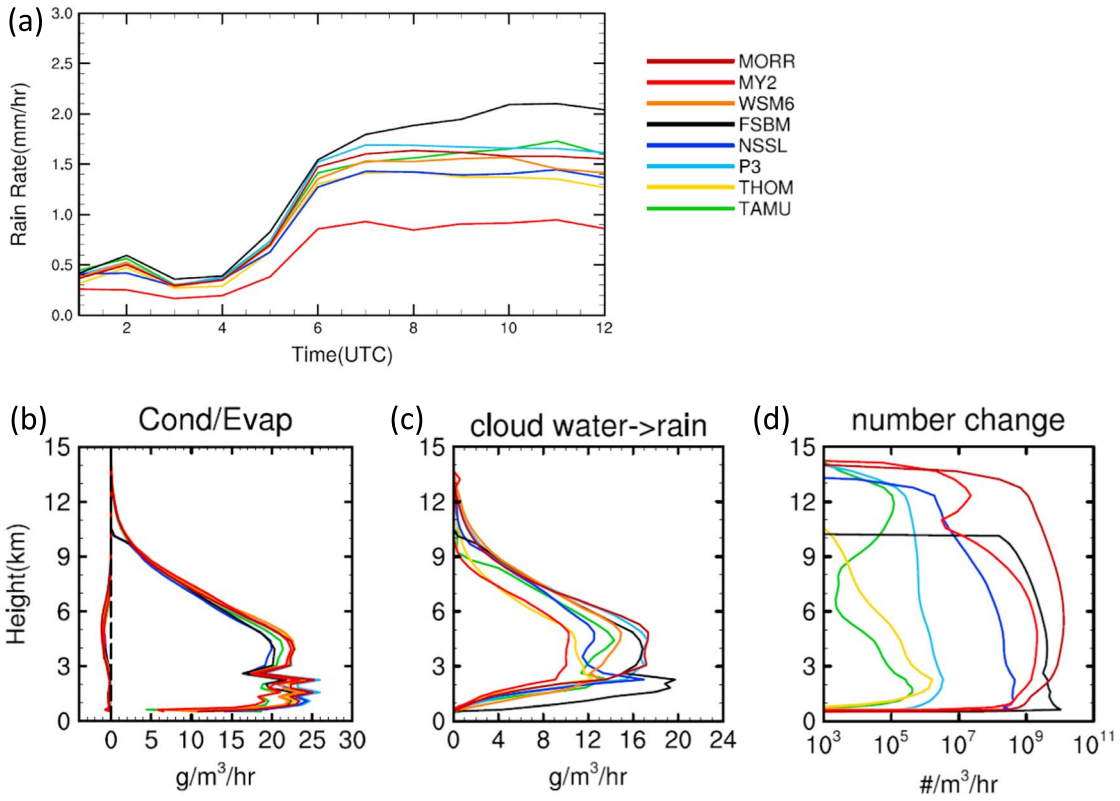

Figure 19. (a) Time series of surface precipitation rate, (b) vertical profiles of condensation and evaporation rates, and (c) mass conversion rates of cloud water to rain water due to collision-coalescence between liquid drops (i.e., autoconversion and collection of droplets by raindrops) from the no-ice simulations; (d) as in Figure 19c, except for cloud droplet number reduction rates (note P3 and THOM only include the reduction from the autoconversion processes since they do not account for cloud droplet number changes due to collection of droplets by raindrops). Figures 19b–19d are averaged for 0800, 0900, and 1000 UTC for updraft points with $w > 2$ m s^{-1} over the entire model domain.

similar, as shown in Figure 19b. Therefore, for warm cloud processes, parameterization improvement should focus on the collision-coalescence processes between liquid drops (including autoconversion and raindrop collection of droplets in the bulk schemes) in order to reduce model uncertainty in simulating precipitation. Note that MY2 is an outlier among the no-ice simulations in that it predicts not only much stronger convection (Figure 17) but also much smaller rain rates (Figure 19a) than the other simulations. The smaller rain rate is associated with smaller rain formation rate (Figure 19b). Much stronger convection compared with the other simulations might be because of the dramatically weakened cold pool intensity (Figure 18a), leading to a more optimal balance between the cold pool and the low-level environmental wind shear, which results in more upright and stronger convection ($C_j/\Delta u$ at 0900 UTC is only about 1.7 for MY2, while others have values of 2.7–5.5).

5. Conclusions and Discussion

A constrained CRM intercomparison study is performed using the same dynamical model (i.e., WRF-ARW) with eight different cloud microphysics schemes including one-moment bulk, two-moment bulk, and bin parameterizations. The primary purpose is to identify specific processes and parameterizations that lead to the large spread in simulated convective cloud properties using different schemes. The first part of the study described in this paper focuses on differences in updraft properties and surface precipitation. Simulations are conducted with eight schemes for a large midlatitude squall line case occurring on 20 May 2011 during the MC3E field experiment. A set of sensitivity tests are conducted to test the roles of ice-related processes and rain evaporation in causing simulation spread and biases compared with observations.

Accumulated surface precipitation in the simulations mostly falls within the observed range provided by ABRFC and bias-corrected Q2 retrievals, with MY2 and THOM as outliers (lower than rainfall observed by

different measurements). Comparison with NEXRAD radar reflectivity shows that the simulations tend to produce a larger region of high radar reflectivity. They also produce a narrower stratiform region with generally overestimated reflectivity, with FSBM and NSSL of no significant estimation. The simulated magnitude of near-surface virtual potential temperature drop associated with the passage of the squall line gust front is similar to observations, but the pressure rise and wind speed peak are less than those observed by Oklahoma Mesonet stations, suggesting that simulated cold pools may be shallower than observed.

Comparisons with a multi-Doppler radar wind field retrieval suggest that simulations generally overestimate updraft velocity, but this overestimation is not found to be as dramatic as was observed for a tropical MCS case from TWP-ICE [*Varble et al*., 2014a]. However, all simulations exhibit decreases in updraft area from lower to upper levels, opposite to the multi-Doppler retrieval trends but qualitatively similar to the RWP retrieval. The multi-Doppler retrieval updraft area could be biased high at upper levels and biased low at low levels because of the retrieval methodology, although the magnitude of the multi-Doppler retrieval agrees with the RWP retrieval. The simulations tend to underestimate updraft area at upper levels, producing small, intense updraft cores aloft regardless of the microphysics scheme. This also occurs in the no-ice simulations. Increasing the horizontal grid-spacing to 200 m increases core size, but not enough to match observations, suggesting that this feature is likely related primarily to nonmicrophysical model aspects such as diffusion and mixing.

Simulated updraft velocity is sensitive to the chosen microphysics scheme, with 6–8 m s^{-1} differences in strong updrafts between the schemes. Differences in simulated updraft intensity correlate well with differences in both simulated buoyancy and low-level vertical PPG; both are small for the WCG (weak convective group; i.e., FSBM and NSSL), while both are large for the SCG (strong convective group; i.e., MORR, MY2, and WSM6). For the simulations with intermediate updraft velocity between the SCG and WCG, either PPG or buoyancy is smaller than SCG values. The magnitude of simulated low-level PPG correlates well with cold pool intensity, which appears to be strongly controlled by evaporation rate. In this squall-line case dominated by upshear-tilted convective updrafts, the rear-inflow jet also contributes to a more optimal convective state and thus may enhance updraft strength. Stronger rear-inflow jet in the SCG than in the WCG appears to lead to a more "optimal" stronger convection RKW state. Condensate loading offsets thermal buoyancy by up to 50% at upper levels, although thermal buoyancy controls buoyancy variability across different schemes. Latent heating differences are the dominant factor in producing differences in thermal buoyancy between the SCG and the WCG.

Ice-related microphysical processes enhance convective strength significantly and are a major contributor to spreads in simulated updraft speed (the upper level updraft speed is reduced by half from the full microphysics runs to the no-ice runs, and the spread in simulated updraft speeds is reduced by more than half). Mechanisms through which ice-related microphysical parameterizations drive the model spread in updraft intensity are (1) increasing simulation differences in evaporation rate and thus cold pool intensity and (2) increasing differences in latent heating and thus buoyancy. Therefore, model spread is increased via feedbacks between ice-phase processes and the dynamics and thermodynamics. Riming heating variability appears to be a contributor to updraft velocity variability. For example, the SCG has the largest peak riming heating rates below 5.5 km altitude where updraft velocity model spread begins to form. But condensation heating and, potentially, deposition heating are also important. For example, the WCG has modest riming heating but relatively weak condensation and deposition rates. However, we cannot rule out the possible contribution to simulated updraft speed variability from the microphysical processes in the warm region of the cloud. For example, large differences in collision-coalescence in the warm region may contribute to the variability of updraft velocity in the full microphysics runs (with ice) because it can change the liquid mass, size, and number concentrations that reach the mixed-phase region, impacting riming and cloud droplet freezing. The lack of clear correlation between updraft intensity and any one latent heating process indicates that several different microphysical processes are important, complexly interacting with one another and feeding back to the dynamics and thermodynamics in complex ways. Isolating the effects of microphysics-dynamics feedbacks from the direct contribution of each process to the spread of updraft velocity can be studied with the "piggyback" approach [*Grabowski*, 2014, 2015] and is a topic for future research.

Stronger convection generally produces larger total condensate mass across schemes, as the SCG has larger total condensate mass than the WCG. The major contributor to total condensate mass in updrafts above 6 km altitude is graupel (or hail for those using hail to represent high-density ice) in most schemes, with THOM as

an outlier having more snow than rimed ice. All bulk schemes predict more cloud water mass than the FSBM bin scheme, possibly associated with larger condensation rates in the bulk schemes.

WSM6 and TAMU produce the most surface precipitation, while MY2 and THOM produce the least. More precipitation in WSM6 and TAMU corresponds to larger total condensate mass than in the other simulations. However, MY2 is an outlier in that it predicts the largest total condensate mass with surface rainfall among the lowest simulated, possibly due to smaller ice particle sizes and graupel terminal velocity. Thus, surface rainfall does not always correlate well with total condensate mass in the updrafts. For THOM, the small rainfall rate is likely a result of the dominance of slower-falling snow over faster-falling graupel in updrafts. Although turning off ice-related microphysics reduces the simulated convective intensity variability, precipitation variability increases mainly because of differences in parameterizing collision-coalescence processes between schemes that are buffered by ice-related processes in the full microphysics runs. Therefore, for warm cloud processes, an emphasis on constraining collision-coalescence processes would significantly reduce model uncertainty in simulating precipitation.

Lastly, we note that the WCG (FSBM and NSSL) happens to employ a prognostic approach for cloud droplet number concentration, while fixed cloud droplet number is used in all of the other schemes. A separate investigation is needed to examine the effects of prognostic versus fixed cloud droplet number concentration on convective strength. Since aerosol and cloud droplet number concentrations used in the simulations are not well justified due to the lack of robust measurements for this case, aerosol effects on updraft intensity could add uncertainty to the results. However, preliminary sensitivity tests show that the primary conclusions of this paper are not impacted by significantly changing the CCN or cloud droplet number concentrations (not shown). A follow-on study is planned for examining aerosol impacts on the squall line using the range of different schemes employed here.

Acknowledgments

This study was supported by the U.S. Department of Energy (DOE) Atmospheric System Research (ASR) Program. The Pacific Northwest National Laboratory (PNNL) is operated for the DOE by Battelle Memorial Institute under contract DE-AC06-76RLO1830. This research used PNNL Institutional Computing resources and also resources at the National Energy Research Scientific Computing Center, which is supported by the Office of Science of the U.S. DOE under contract DE-AC02-05CH1123. Bin Han and Chen were supported by the National Basic Research Program of China (2013CB430105). Varble was supported by U.S. DOE ASR DE-SC0008678. Morrison was supported by U.S. DOE ASR DE-SC0008648. Morrison and Varble were also supported by U.S. DOE ASR DE-SC0016476. Giangrande is an employee of Brookhaven Science Associates LLC under contract DE-AC02-98CH10886 with the U.S. DOE. The National Center for Atmospheric Research is sponsored by the U.S. National Science Foundation. Y. Wang is supported by the ROSES14-ACMAP project. The PNNL Institutional Computing (PIC) resources were used for the model simulations of this study. The simulation data are available at the PNNL PIC and can be obtained by contacting the corresponding author, Jiwen Fan (jiwen.fan@pnnl.gov). We also acknowledge the Atmospheric Radiation Measurement (ARM) Climate Research Facility, a user facility of the U. S. DOE, Office of Science, sponsored by the Office of Biological and Environmental Research, and support from the ASR program of that office. DOE ARM data sets used in this study can be obtained from the ARM archive at http://www.arm.gov and ARM External Data Center at https://www.arm.gov/xdc/. The Oklahoma MESONET data are downloaded from https://www.mesonet.org/index.php/weather/category/past_data_files with the help of Lulin Xue and Xia Chu at NCAR.

References

Arakawa, A. (2004), The cumulus parameterization problem: Past, present, and future, *J. Clim.*, *17*, 2493–2525.

Atmospheric Radiation Measurement (ARM) Climate Research Facility (2010), Updated hourly. C-band ARM precipitation radar (CSAPRSUR). Compiled by N. Bharadwaj, D. Nelson, B. Isom, J. Hardin, I. Lindenmaier and S. Collis. Atmospheric Radiation Measurement (ARM) Climate Research Facility Data Archive, Oak Ridge, Tenn, doi:10.5439/1025170.

Baldauf, M., A. Seifert, J. Forstner, D. Majewski, M. Raschendorfer, and T. Reinhardt (2011), Operational convective-scale numerical weather prediction with the COSMO model: Description and sensitivities, *Mon. Weather Rev.*, *139*, 3887–3905.

Benjamin, T. B. (1968), Gravity currents and related phenomena, *J. Fluid Mech.*, *31*, 209–248.

Bigg, E. K. (1953), The formation of atmospheric ice crystals by the freezing of droplets, *Q. J. R. Meteorol. Soc.*, *79*(342), 510–519, doi:10.1002/qj.49707934207.

Bryan, G. H., and H. Morrison (2012), Sensitivity of a simulated squall line to horizontal resolution and parameterization of microphysics, *Mon. Weather Rev.*, *140*, 202–225, doi:10.1175/MWR-D-11-00046.1.

Bryan, G. H., J. C. Wyngaard, and J. M. Fritsch (2003), Resolution requirements for the simulation of deep moist convection, *Mon. Weather Rev.*, *131*, 2394–2416.

Bryan, G. H., J. C. Knievel, and M. D. Parker (2006), A multimodel assessment of RKW theory's relevance to squall-line characteristics, *Mon. Weather Rev.*, *134*(10), 2772–2792, doi:10.1175/mwr3226.1.

Chen, F., and J. Dudhia (2001), Coupling an advanced land surface-hydrology model with the Penn State-NCAR MM5 modeling system. Part I: Model implementation and sensitivity, *Mon. Weather Rev.*, *129*, 569–585.

Cooper, W. A. (1986), Ice initiation in natural clouds, *Meteorol. Monogr.*, *21*, 29–32.

Cotton, W. R., G. J. Tripoli, R. M. Rauber, and E. A. Mulvihill (1986), Numerical simulation of the effects of varying ice crystal nucleation rates and aggregation processes on orographic snowfall, *J. Climate Appl. Meteor.*, *25*, 1658–1680.

DeMott, P. J., M. P. Meyers, and W. R. Cotton (1994), Parameterization and impact of ice initiation processes relevant to numerical model simulations of cirrus clouds, *J. Atmos. Sci.*, *51*, 77–90.

Fan, J., D. Rosenfeld, Y. Ding, L. R. Leung, and Z. Li (2012), Potential aerosol indirect effects on atmospheric circulation and radiative forcing through deep convection, *Geophys. Res. Lett.*, *39*, L09806, doi:10.1029/2012GL051851.

Fan, F., L. R. Leung, D. Rosenfeld, Q. Chen, Z. Li, J. Zhang, and H. Yan (2013), Microphysical effects determine macrophysical response for aerosol impact on deep convective clouds, *P. Natl. Acad. Sci. U.S.A.*, *110*, E4581E–E44590, doi:10.1073/pnas.1316830110.

Fan, J., Y.-C. Liu, K.-M. Xu, K. North, S. Collis, X. Dong, G. J. Zhang, Q. Chen, P. Kollias, and S. J. Ghan (2015), Improving representation of convective transport for scale-aware parameterization: 1. Convection and cloud properties simulated with spectral bin and bulk microphysics, *J. Geophys. Res. Atmos.*, *120*, 3485–3509, doi:10.1002/2014JD022142.

Ferrier, B. S. (1994), A two-moment multiple-phase four-class bulk ice scheme. Part I: Description, *J. Atmos. Sci.*, *51*, 249–280.

Fiebrich, C. A., D. L. Grimsley, R. A. McPherson, K. A. Kesler, and G. R. Essenberg (2006), The value of routine site visits in managing and maintaining quality data from the Oklahoma Mesonet, *J. Atmos. Oceanic Technol.*, *23*, 406–416, doi:10.1175/JTECH1852.1.

Fridlind, A. M., et al. (2012), A comparison of TWP-ICE observational data with cloud-resolving model results, *J. Geophys. Res.*, *117*, D05204, doi:10.1029/2011JD016595.

Fridlind, A. M., et al. (2017), Derivation of aerosol profiles for MC3E convection studies and use in simulations of the 20 May squall line case, *Atmos. Chem. Phys.*, *17*, 5947–5972, doi:10.5194/acp-17-5947-2017.

Giangrande, S. E., and A. V. Ryzhkov (2008), Estimation of rainfall based on the results of polarimetric echo classification, *J. Appl. Meteorol. Climatol.*, *47*, 2445–2462, doi:10.1175/2008JAMC1753.1.

Giangrande, S. E., S. Collis, J. Straka, A. Protat, C. Williams, and S. Krueger (2013), A summary of convective-core vertical velocity properties using ARM UHF wind profilers in Oklahoma, *J. Appl. Meteorol. Climatol.*, *52*, 2278–2295.
Giangrande, S. E., S. Collis, A. K. Theisen, and A. Tokay (2014), Precipitation estimation from the ARM distributed radar network during the MC3E campaign, *J. Appl. Meteorol. Climatol.*, *53*, 2130–2147.
Giangrande, S. E., T. Toto, M. P. Jensen, M. J. Bartholomew, Z. Feng, A. Protat, C. R. Williams, C. Schumacher, and L. Machado (2016), Convective cloud vertical velocity and mass-flux characteristics from radar wind profiler observations during GoAmazon2014/5, *J. Geophys. Res. Atmos.*, *121*, 12,891–12,913, doi:10.1002/2016JD025303.
Gourley, J. J., S. E. Giangrande, Y. Hong, Z. Flaming, T. Schuur, and J. A. Vrugt (2010), Impacts of polarimetric radar observations on hydrologic simulation, *J. Hydrometeorol.*, *11*, 781–796, doi:10.1175/2010JHM1218.1.
Grabowski, W. W. (2014), Extracting microphysical impacts in large-eddy simulations of shallow convection, *J. Atmos. Sci.*, *71*, 4493–4499, doi:10.1175/JAS-D-14-0231.1.
Grabowski, W. W. (2015), Untangling microphysical impacts on deep convection applying a novel modeling methodology, *J. Atmos. Sci.*, *72*, 2446–2464, doi:10.1175/JAS-D-14-0307.1.
Grabowski, W. W., and H. Morrison (2017), Modeling condensation in deep convection, *J. Atmos. Sci.*, *74*, 2247–2267, doi:10.1175/JAS-D-16-0255.1.
Hong, S.-Y., and J.-O. J. Lim (2006), The WRF single-moment 6-class microphysics scheme (WSM6), *J. Korean Meteorol. Soc.*, *42*, 129–151.
Hong, S.-Y., Y. Noh, and J. Dudhia (2006), A new vertical diffusion package with an explicit treatment of entrainment processes, *Mon. Weather Rev.*, *134*, 2318–2341.
Houze, R. A. (2014), *Cloud Dynamics*, 2nd ed., pp. 165–166, Elsevier, Seattle, Wash.
Iacono, M. J., J. S. Delamere, E. J. Mlawer, M. W. Shephard, S. A. Clough, and W. D. Collins (2008), Radiative forcing by long-lived greenhouse gases: Calculations with the AER radiative transfer models, *J. Geophys. Res.*, *113*, D13103, doi:10.1029/2008JD009944.
Jensen, M., et al. (2016), The Midlatitude Continental Convective Clouds Experiment (MC3E), *Bull. Am. Meteorol. Soc.*, *97*, 1667–1686, doi:10.1175/BAMS-D-14-00228.1.
Kain, J. S. (2004), The Kain-Fritsch convective parameterization: An update, *J. Appl. Meteorol.*, *43*, 170–181.
Khain, A. P. (2009), Notes on state-of-art investigations of aerosol effects on precipitation: A critical review, *Environ. Res. Lett.*, *4*, 015004, doi:10.1088/1748-9326/4/1/015004.
Khain, A. P., et al. (2015), Representation of microphysical processes in cloud-resolving models: Spectral (bin) microphysics versus bulk parameterization, *Rev. Geophys.*, *53*, 247–322, doi:10.1002/2014RG000468.
Kumar, V. V., C. Jakob, A. Protat, C. R. Williams, and P. T. May (2015), Mass-flux characteristics of tropical cumulus clouds from wind profiler observations at Darwin, Australia, *J. Atmos. Sci.*, *72*, 1837–1855.
Kumjian, M. R., S. Mishra, S. E. Giangrande, T. Toto, A. V. Ryzhkov, and A. Bansemer (2016), Polarimetric radar and aircraft observations of saggy bright bands during MC3E, *J. Geophys. Res. Atmos.*, *121*, 3584–3607, doi:10.1002/2015JD024446.
Lebo, Z. J., and J. H. Seinfeld (2011), Theoretical basis for convective invigoration due to increased aerosol concentration, *Atmos. Chem. Phys.*, *11*, 5407–5429, doi:10.5194/acp-11-5407-2011.
Lebo, Z. J., and H. Morrison (2015), Effects of horizontal and vertical grid spacing on mixing in simulated squall lines and implications for convective strength and structure, *J. Atmos. Sci.*, *143*, 4355–4375.
Li, G. H., Y. Wang, and R. Zhang (2008), Implementation of a two-moment bulk microphysics scheme to the WRF model to investigate aerosol-cloud interaction, *J. Geophys. Res.*, *113*, D15211, doi:10.1029/2007JD009361.
Li, X., W.-K. Tao, A. P. Khain, J. Simpson, and D. E. Johnson (2009a), Sensitivity of a cloud-resolving model to bulk and explicit bin microphysical schemes. Part I: Validation with a PRE-STORM case, *J. Atmos. Sci.*, *66*, 3–21, doi:10.1175/2008JAS2646.1.
Li, X., W.-K. Tao, A. P. Khain, J. Simpson, and D. E. Johnson (2009b), Sensitivity of a cloud-resolving model to bulk and explicit bin microphysical schemes. Part II: Cloud microphysics and storm dynamics interactions, *J. Atmos. Sci.*, *66*, 22–40.
Mansell, E. R., C. L. Ziegler, and E. C. Bruning (2010), Simulated electrification of a small thunderstorm with two-moment bulk microphysics, *J. Atmos. Sci.*, *67*, 171–194, doi:10.1175/2009JAS2965.1.
Marinescu, P. J., S. C. van den Heever, S. M. Saleeby, and S. M. Kreidenweis (2016), The microphysical contributions to and evolution of latent heating profiles in two MC3E MCSs, *J. Geophys. Res. Atmos.*, *121*, 7913–7935, doi:10.1002/2016JD024762.
Mather, J. H., and J. W. Voyles (2013), The ARM climate research facility: A review of structure and capabilities, *Bull. Am. Meteorol. Soc.*, *94*, 377–392, doi:10.1175/BAMS-D-11-00218.1.
Meng, Z., F. Zhang, P. Markowski, D. Wu, and K. Zhao (2012), A modeling study on the development of a bowing structure and associated rear inflow within a squall line over South China, *J. Atmos. Sci.*, *69*(4), 1182–1207, doi:10.1175/JAS-D-11-0121.1.
Meyers, M. P., P. J. DeMott, and W. R. Cotton (1992), New primary ice-nucleation parameterizations in an explicit cloud model, *J. Appl. Meteorol.*, *31*, 708–721.
Milbrandt, J. A., and M. K. Yau (2005a), A multimoment bulk microphysics parameterization. Part I: Analysis of the role of the spectral shape parameter, *J. Atmos. Sci.*, *62*, 3051–3064.
Milbrandt, J. A., and M. K. Yau (2005b), A multimoment bulk microphysics parameterization. Part II: A proposed three-moment closure and scheme description, *J. Atmos. Sci.*, *62*, 3065–3081.
Milbrandt, J. A., and R. McTaggart-Cowan (2010), Sedimentation-induced errors in bulk microphysics schemes, *J. Atmos. Sci.*, *67*, 3931–3948, doi:10.1175/2010JAS3541.1.
Milbrandt, J. A., and H. Morrison (2016), Parameterization of cloud microphysics based on the prediction of bulk ice particle properties. Part III: Introduction of multiple free categories, *J. Atmos. Sci.*, *73*, 975–995, doi:10.1175/JAS-D-15-0204.1.
Milbrandt, J. A., A. Glazer, and D. Jacob (2012), Predicting the snow-to-liquid ratio of surface precipitation using a bulk microphysics scheme, *Mon. Weather Rev.*, *140*, 2461–2476, doi:10.1175/MWR-D-11-00286.1.
Morrison, H., and J. A. Milbrandt (2015), Parameterization of cloud microphysics based on the prediction of bulk ice particle properties. Part I: Scheme description and idealized tests, *J. Atmos. Sci.*, *72*, 287–311, doi:10.1175/JAS-D-14-0065.1.
Morrison, H., J. A. Curry, and V. I. Khvorostyanov (2005), A new double-moment microphysics parameterization for application in cloud and climate models. Part I: Description, *J. Atmos. Sci.*, *62*, 1665–1677, doi:10.1175/JAS3446.1.
Morrison, H., G. Thompson, and V. Tatarskii (2009), Impact of cloud microphysics on the development of trailing stratiform precipitation in a simulated squall line: Comparison of one- and two-moment schemes, *Mon. Weather Rev.*, *137*, 991–1007, doi:10.1175/2008MWR2556.1.
Morrison, H., S. A. Tessendorf, K. Ikeda, and G. Thompson (2012), Sensitivity of a simulated midlatitude squall line to parameterization of raindrop breakup, *Mon. Weather Rev.*, *140*, 2437–2460, doi:10.1175/MWR-D-11-00283.1.
North, K. W., M. Oue, P. Kollias, S. E. Giangrande, S. Collis, and C. K. Potvin (2017), Vertical air motion retrievals in deep convective clouds using the ARM scanning radar network in Oklahoma during MC3E, *Atmos. Meas. Tech.*, *10*, 2785–2806, doi:10.5194/amt-2016-269.

Petersen, W. A., and M. Jensen (2012), The NASA-GPM and DOE-ARM Midlatitude Continental Convective Clouds Experiment (MC3E), *Int. J. Appl. Earth Obs.*, *24*, 12–18.
Phillips, V. T. J., L. J. Donner, and S. T. Garner (2007), Nucleation processes in deep convection simulated by a cloud-system-resolving model with double-moment bulk microphysics, *J. Atmos. Sci.*, *64*, 738–761.
Pruppacher, H. R., and J. D. Klett (1997), *Microphysics of Clouds and Precipitation*, 2nd ed., 914 pp., Oxford Press, Oxford.
Randall, D. A., et al. (2003), Confronting models with data: The GEWEX cloud systems study, *Bull. Am. Meteorol. Soc.*, *84*(4), 455–469, doi:10.1175/BAMS-84-4-455.
Redelsperger, J. L., et al. (2000), A GCSS model intercomparison for a tropical squall line observed during TOGA-COARE. Part I: CRM results, *Q. J. R. Meteorol. Soc.*, *126*, 823–863.
Rotunno, R., J. B. Klemp, and M. L. Weisman (1988), A theory for strong, long-lived squall lines, *J. Atmos. Sci.*, *45*, 463–485, doi:10.1175/1520-0469(1988)045,0463.
Saleeby, S. M., S. C. van den Heever, P. J. Marinescu, S. M. Kreidenweis, and P. J. DeMott (2016), Aerosol indirect effects on the anvil characteristics of mesoscale convective systems, *J. Geophys. Res. Atmos.*, *121*, 10,880–10,901, doi:10.1002/2016JD025082.
Stenz, R., X. Dong, B. Xi, and B. Kuligowski (2014), Assessment of SCaMPR and NEXRAD Q2 precipitation estimates using Oklahoma Mesonet observations, *J. Hydrometeorol.*, *15*(6), 2484–2500.
Suhas, E., and G. J. Zhang (2015), Evaluating convective parameterization closures using cloud-resolving model simulation of tropical deep convection, *J. Geophys. Res. Atmos.*, *120*, 1260–1277, doi:10.1002/2014JD022246.
Takemi, T. (2007), Environmental stability control of the intensity of squall lines under low-level shear conditions, *J. Geophys. Res.*, *112*, D24110, doi:10.1029/2007JD008793.
Tao, W.-K., D. Wu, T. Matsui, C. Peters-Lidard, S. Lang, A. Hou, M. Rienecker, W. Petersen, and M. Jensen (2013), Precipitation intensity and variation during MC3E: A numerical modeling study, *J. Geophys. Res. Atmos.*, *118*, 7199–7218, doi:10.1002/jgrd.50410.
Tao, W.-K., D. Wu, S. Lang, J.-D. Chern, C. Peters-Lidard, A. Fridlind, and T. Matsui (2016), High-resolution NU-WRF simulations of a deep convective-precipitation system during MC3E: Further improvements and comparisons between Goddard microphysics schemes and observations, *J. Geophys. Res. Atmos.*, *121*, 1278–1305, doi:10.1002/2015JD023986.
Thompson, G., R. M. Rasmussen, and K. Manning (2004), Explicit forecasts of winter precipitation using an improved bulk microphysics scheme. Part I: Description and sensitivity analysis, *Mon. Weather Rev.*, *132*, 519–542.
Thompson, G., P. R. Field, R. M. Rasmussen, and W. D. Hall (2008), Explicit forecasts of winter precipitation using an improved bulk microphysics scheme. Part II: Implementation of a new snow parameterization, *Mon. Weather Rev.*, *136*, 5095–5115.
Tompkins, A. M. (2001), Organization of tropical convection in low vertical wind shears: The role of cold pools, *J. Atmos. Sci.*, *58*, 1650–1672, doi:10.1175/1520-0469(2001)058<1650OOTCIL>2.0.CO;2.
Torri, G., Z. Kuang, and Y. Tian (2015), Mechanisms for convection triggering by cold pools, *Geophys. Res. Lett.*, *42*, 1943–1950, doi:10.1002/2015GL063227.
Van den Heever, S. C., and W. R. Cotton (2004), The impact of hail size on simulated supercell storms, *J. Atmos. Sci.*, *61*, 1596–1609.
Van Lier-Walqui, M., A. M. Fridlind, A. S. Ackerman, S. Collis, J. Helmus, D. R. Macgorman, K. North, P. Kollias, and D. J. Posselt (2016), On polarimetric radar signatures of deep convection for model evaluation, columns of specific differential phase observed during MC3E, *Mon. Weather Rev.*, *144*, 737–758, doi:10.1175/MWR-D-15-0100.1.
Varble, A., A. M. Fridlind, E. J. Zipser, A. S. Ackerman, J.-P. Chaboureau, J. Fan, A. Hill, S. A. McFarlane, J.-P. Pinty, and B. Shipway (2011), Evaluation of cloud-resolving model intercomparison simulations using TWP-ICE observations: Precipitation and cloud structure, *J. Geophys. Res.*, *116*, D12206, doi:10.1029/2010JD015180.
Varble, A., E. J. Zipser, A. M. Fridlind, P. Zhu, A. S. Ackerman, J.-P. Chaboureau, S. Collis, J. Fan, A. Hill, and B. Shipway (2014a), Evaluation of cloud-resolving and limited area model intercomparison simulations using TWP-ICE observations: 1. Deep convective updraft properties, *J. Geophys. Res. Atmos.*, *119*, 13,891–13,918, doi:10.1002/2013JD021371.
Varble, A., E. J. Zipser, A. M. Fridlind, P. Zhu, A. S. Ackerman, J.-P. Chaboureau, J. Fan, A. Hill, B. Shipway, and C. Williams (2014b), Evaluation of cloud-resolving and limited area model intercomparison simulations using TWP-ICE observations: 2. Precipitation microphysics, *J. Geophys. Res. Atmos.*, *119*, 13,919–13,945, doi:10.1002/2013JD021372.
Wang, J., X. Dong, B. Xi, and A. J. Heymsfield (2016), Investigation of liquid cloud microphysical properties of deep convective systems: 1. Parameterization of raindrop size distribution and its application for stratiform rain estimation, *J. Geophys. Res. Atmos.*, *121*, 10,739–10,760, doi:10.1002/2016JD024941.
Wang, Y., Q. Wan, W. Meng, F. Liao, H. Tan, and R. Zhang (2011), Long-term impacts of aerosols on precipitation and lightning over the Pearl River Delta megacity area in China, *Atmos. Chem. Phys.*, *11*(23), 12,421–12,436.
Wang, Y., J. Fan, R. Zhang, L. R. Leung, and C. Franklin (2013), Improving bulk microphysics parameterizations in simulations of aerosol effects, *J. Geophys. Res. Atmos.*, *118*, 5361–5379, doi:10.1002/jgrd.50432.
Weisman, M. L. (1992), The role of convectively generated rear-inflow jets in the evolution of long-lived mesoconvective systems, *J. Atmos. Sci.*, *49*, 1826–1847.
Weisman, M. L., and R. Rotunno (2004), "a theory for strong long-lived squall lines" revisited, *J. Atmos. Sci.*, *61*(4), 361–382, doi:10.1175/1520-0469(2004)061.
Whiton, R. C., P. L. Smith, S. G. Bigler, K. E. Wilk, and A. C. Harbuck (1998), History of operational use of weather radar by U.S. weather services. Part II: Development of operational Doppler weather radars, *Weather Forecasting*, *13*, 244–252, doi:10.1175/1520-0434(1998)013<0244:HOOUOW>2.0.CO;2.
Xie, S., Y. Zhang, S. E. Giangrande, M. P. Jensen, R. McCoy, and M. Zhang (2014), Interactions between cumulus convection and its environment as revealed by the MC3E sounding array, *J. Geophys. Res. Atmos.*, *119*, 11,784–11,808, doi:10.1002/2014JD022011.
Xu, K. M., et al. (2002), An intercomparison of cloud-resolving models with the atmospheric radiation measurement summer 1997 intensive observation period data, *Q. J. R. Meteorol. Soc.*, *128*(580), 593–624.
Young, C. B., A. A. Bradley, W. F. Krajewski, A. Kruger, and M. L. Morrissey (2000), Evaluating NEXRAD multisensor precipitation estimates for operational hydrologic forecasting, *J. Hydrometeorol.*, *1*, 241–254, doi:10.1175/1525-7541(2000)001<0241:ENMPEF>2.0.CO;2.
Zhang, J., K. Howard, and J. J. Gourley (2005), Constructing three-dimensional multiple-radar reflectivity mosaics: Examples of convective storms and stratiform rain echoes, *J. Atmos. Oceanic Technol.*, *22*, 30–42, doi:10.1175/JTECH-1689.1.
Zhang, J., et al. (2011), National mosaic and multi-sensor QPE (NMQ) system: Description, results, and future plans, *Bull. Am. Meteorol. Soc.*, *92*, 1321–1338, doi:10.1175/2011BAMS-D-11-00047.1.
Zhu, P., J. Dudhia, P. R. Field, A. Fridlind, A. Varble, E. Zipser, J. Petch, M. Chen, and Z. Zhu (2012), A limited area model (LAM) intercomparison study of a TWP-ICE active monsoon mesoscale convective event, *J. Geophys. Res.*, *117*, D11208, doi:10.1029/2011JD016447.